

Article

Metallogenic Mechanism of Carlin-Type Gold Deposit in Zhen'an-Xunyang Basin, in the South Qinling of China: Constraints of In Situ Trace Elements and S Isotopes from Newly Discovered Wangzhuang Gold Deposit

Wuyi Meng ¹, Jiajun Liu ^{2,3,*}, Huanhuan Wu ^{1,3}, Zhen Zhang ¹, Weidong Tang ¹, Yongbao Gao ¹, Liyong Wei ¹, Bin Jia ¹, Xin Zheng ¹ and Ningbo Liu ¹

¹ Xi'an Center of Mineral Resources Survey, China Geological Survey, Xi'an 710199, China; wuyi4960@163.com (W.M.); whhcugb@163.com (H.W.); 13109576962@163.com (Z.Z.); tangweidong@mail.cgs.gov.cn (W.T.); gaoyongbao2006@126.com (Y.G.); weiliyong@mail.cgs.gov.cn (L.W.); jiabin1913@163.com (B.J.); zhengxin081692@163.com (X.Z.); can3218517@163.com (N.L.)

² State Key Laboratory of Geological Processes and Mineral Resources, China University of Geosciences, Beijing 100083, China

³ School of Earth Sciences, China University of Geosciences (Beijing), Beijing 100083, China

* Correspondence: liujiajun@cugb.edu.cn

Abstract: The Zhen'an-Xunyang Basin is a late Paleozoic rifted basin with a series of Au-Hg-Sb deposits that have been found, mostly along the Nanyangshan fault. Recently discovered large- and medium-sized gold deposits such as the Xiaohe and Wangzhuang deposits exhibit typical characteristics of Carlin-type gold deposits. Therefore, it is imperative to select a typical deposit for an in-depth study of its metallogenic mechanism to support future prospecting efforts targeting the Carlin-type gold deposits within the area. Based on detailed field investigation and microphotographic observation, four ore-forming stages are identified: I, low-sulfide quartz stage, characterized by euhedral, subhedral pyrite, and fine veins of quartz injected parallel to the strata; II, arsenopyrite–arsenian pyrite–quartz stage, the main mineralization stage characterized by strongly silicified zones of reticulated quartz, disseminated arsenopyrite, fine-grained pyrite; III, low-sulfide quartz stage, characterized by large quartz veins cutting through the ore body or fine veins of quartz; IV, carbonate–quartz stage, characterized by the appearance of a large number of calcite veins. In situ analysis of trace elements and S isotopes of typical metal sulfides was carried out. The results show significant variations in the trace element compositions of metal sulfides in different stages, among which the main mineralization stage differs notably from those of the Au- and As-low surrounding strata. In situ S isotope analysis reveals $\delta^{34}\text{S}$ values ranging from 15.78‰ to 28.71‰ for stage I metal sulfides, 5.52‰ to 11.22‰ for stage II, and 0.3‰ to 5.25‰ for stage III, respectively, revealing a gradual decrease in S isotopic values from the pre-mineralization stage to post-mineralization stage, similar to those observed in the Xiaohe gold deposit. These features indicate a distinct injection of relatively low ^{34}S hydrothermal fluids during the mineralization process. The element anomalies of the 1:50,000 stream sediment in the region revealed ore-forming element zonation changing in W→Au (W)→Hg, Sb (Au) anomalies from west to east, manifested by the discovery of tungsten, gold, and mercury–antimony deposits in the area. Moreover, conspicuous Cr-Ni-Ti-Co-Mo anomalies were observed on the western side of the Wangzhuang and Xiaohe gold deposits, indicating a potential concealed pluton related to these deposits. These lines of evidence point to a magmatic–hydrothermal origin for the Carlin-type gold deposits in this area. Furthermore, hydrothermal tungsten deposits, Carlin-type gold deposits, and low-temperature hydrothermal mercury–antimony deposits in this region are probably controlled by the same magma–hydrothermal system.

Keywords: pyrite; trace elements; S isotope; the Wangzhuang gold deposit; the Zhen'an-Xunyang basin



Citation: Meng, W.; Liu, J.; Wu, H.; Zhang, Z.; Tang, W.; Gao, Y.; Wei, L.; Jia, B.; Zheng, X.; Liu, N. Metallogenic Mechanism of Carlin-Type Gold Deposit in Zhen'an-Xunyang Basin, in the South Qinling of China: Constraints of In Situ Trace Elements and S Isotopes from Newly Discovered Wangzhuang Gold Deposit. *Minerals* **2023**, *13*, 1459. <https://doi.org/10.3390/min13111459>

Academic Editor: Stefano Salvi

Received: 18 October 2023

Revised: 14 November 2023

Accepted: 16 November 2023

Published: 20 November 2023



Copyright: © 2023 by the authors. Licensee MDPI, Basel, Switzerland. This article is an open access article distributed under the terms and conditions of the Creative Commons Attribution (CC BY) license (<https://creativecommons.org/licenses/by/4.0/>).

1. Introduction

The Carlin-type gold deposits (CTDs), one of the most significant hydrothermal gold deposits, have attracted considerable attention due to their extensive metallogenic scale and promising exploration potential [1,2]. In recent years, many studies have revealed that some geological and geochemical characteristics of these gold deposits in China differ from those of the most typical Carlin-type gold deposits in Nevada, USA. Consequently, some scholars named them as Carlin-like gold deposits [3–6]. Taking China as an example, there are hundreds of Carlin-type gold deposits with accumulated industrial reserves totaling approximately 2000 tons [7], primarily concentrated in the Shaanxi, Gansu, and Sichuan regions (Qinling Mountains), as well as Yunnan, Guizhou, and Guangxi regions [5,8–10]. Among them, the Qinling orogenic belt hosts two world-class Carlin-type gold deposits, the Jinlongshan and Zhaishang gold deposits, which are regarded as two of the most important Carlin-type gold metallogenic belts in China.

Many Carlin-like, Carlin-type gold deposits have been discovered in the Qinling metallogenic belt, mainly distributed in the west and south of the Qinling metallogenic belt (Figure 1). Since the ore-forming fluid characteristics of some gold deposits in west Qinling are between orogenic gold deposits and Carlin-type gold deposits [3,4,7–9,11], the classification of their ore-forming types has long been debated. It is acknowledged that the fluids and metal sources of orogenic gold deposits are mainly from regional-scale metamorphism instead of magmatic activity, and thus there is no large area of element zonation around these deposits [11–13]. In contrast, Carlin-type gold deposits generally show a close relationship with magmatic activity, which is represented by the inconsistency of fluid sources in multiple stages and different stages of mineralization [14–17]. As far as the present research is concerned, the origin of gold deposits in south Qinling has a unified understanding, and there are Carlin-type gold deposits represented by Jinlongshan [18–20]. However, the research on the source of ore-forming materials and the metallogenic mechanism of a series of Carlin-type gold deposits in the central part of the Zhen’an-Xunyang Basin (ZXB) is relatively weak, which restricts the study of the metallogenic system theory of Carlin-type gold deposits and low-temperature hydrothermal Hg-Sb deposits in the area. This lack of research may hinder our understanding of the geological processes that led to the formation of these deposits and their potential for further exploration and development.

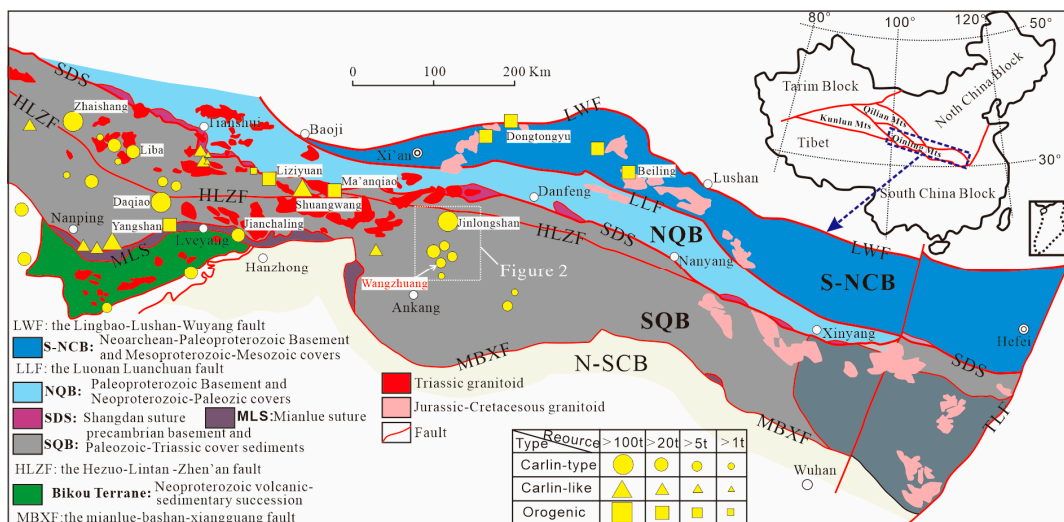


Figure 1. Tectonic divisions and gold distribution in the Qinling orogenic belt (tectonic framework modified after Dong and Santosh [21]; gold distribution and classification compiled after Chen, Liu, and Ma [4,8,20]).

The ZXB is an early Paleozoic sedimentary basin located in the south Qinling orogenic belt (SQB). It comprises a series of carbonate and fine clastic sedimentary formations. The

distribution of deposits in this area is mainly controlled by the Nanyangshan fault situated in the middle of the basin [22]. The basin is renowned for its polymetallic mineralization, including gold, mercury, antimony, lead, and zinc [23–26]. In particular, it hosts the Jinlongshan super-large Carlin-type gold deposit in its northern region [20,26] and a series of sedimentary exhalative (Sedex) lead–zinc deposits in its southern region [22]. Additionally, the central part of this basin lies on the Gongguan and Qingtonggou super-large mercury–antimony deposits, which have become significant metallogenic belts for mercury (antimony) mineralization in China [27–29]. Several gold deposits, such as Xiaohe (>20 t, by Zijin Mining, Xiamen, China), Laojunmiao (>18 t, by Shaanxi Geology and Mining First Geological Team Co., LTD, Xi’an, China), Huijiagou (>5 t, by Shaanxi Geology and Mining First Geological Team Co., LTD, Xi’an, China), and Wangzhuang (>2.5 t, by Xi’an Center of Mineral Resources Survey, China Geological Survey, Xi’an, China), have been discovered within this Hg-Sb metallogenic belt, forming a gold-dominated Hg-Sb-Pb-Zn polymetallic metallogenic belt (Figure 2).

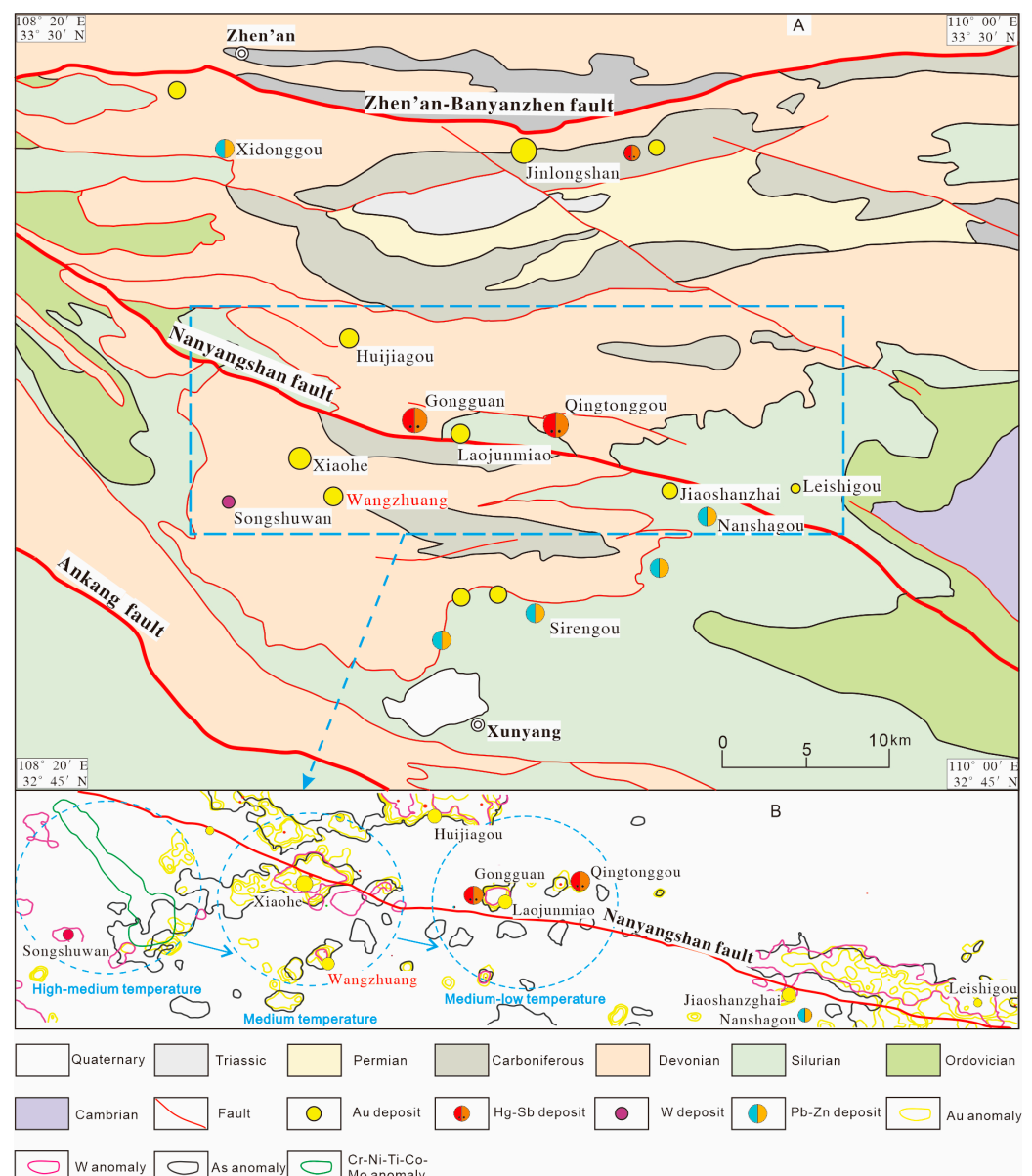


Figure 2. (A) Geologic map of the Zhen’an-Xunyang Basin (geologic framework modified after Zhang [27]); (B) simplified geological map with geochemical anomalies of stream sediments and the locations of related deposits.

The previous research primarily focused on the fundamental geological characteristics of the deposits; however, the properties and sources of ore-forming fluids have not been well constrained. In this study, we selected the Wangzhuang gold deposit, which is situated at the transition of the entire tungsten and mercury–antimony metallogenic belt, as the research object. Based on comprehensive field investigations, multi-stage alteration characteristics of the Wangzhuang gold deposit are identified. Combining detailed mineralogical, mineral geochemical, and in situ S isotopic studies on metal sulfides from each stage, we further constrained the fluid characteristics and ore-forming materials sources, and discuss the genetic mechanism of Carlin-type gold deposits in this region.

2. Regional Geology

The Qinling orogenic belt (QOB) is located at the junction of the collision between the North China Block and the South China Block. It is an important part of the Central Asian Orogenic Belt (CAOB) and a compound continental orogenic belt with long-term development and evolution [21,30,31]. From north to south, the QOB can be divided into four units, namely the southern margin of the North China Block (S-NCB), the North Qinling Block (NQB), the South Qinling Block (SQB) and the northern margin of the South China Block (N-SCB) by the Lingbao–Lushan–Wuyang fault (LWF), Shangdan suture (SDS), and Mianluo–Bashan–Xiangguang fault (MBXF) (Figure 1) [21,31,32]. The QOB represents a significant metallogenic belt for non-ferrous metals and precious metals in China [14,33]. Over the past three decades, numerous large and super-large gold deposits have been discovered, e.g., the Zhaishang, Yangshan, Dashui, Jinlongshan, and Baguamiao deposits. More than 90% of the gold deposits in the Qinling area are hosted by Devonian strata [3,14], which mainly consist of epimetamorphic rock or sedimentary rock. Notably, most of these deposits have been found to have a close spatial and temporal relationship with magmatic activities [14,20,34].

The Zhen'an-Xunyang Basin is a late Paleozoic rifted basin located in the middle of south Qinling's secondary tectonic belt, bounded by the Ankang fault to the south and the Zhen'an-Banyanzhen fault to the north (Figures 1 and 2A). The tectonic framework in this area is primarily influenced by the Indosinian collision orogeny and Yanshanian intracontinental orogeny. From north to south, the ZXB can be divided into three structural units: Jinjiling synclinorium, Gongguan–Huilong anticlinorium, and Nanyangshan synclinorium. These structures also control the distribution of metal minerals in this region, with the predominance of Au-Sb-Hg deposits in the north, Hg-Sb-Au deposits in the middle, and Pb-Zn deposits in the south [35]. This research focuses on the Wangzhuang Carlin-type gold deposit located within the central part of the ZXB.

3. Geological Characteristics of the Deposit

3.1. Ore Geology

The Wangzhuang gold deposit is located in the middle of the late Paleozoic Zhen'an-Xunyang sedimentary basin. The gold deposits surrounding the Nanyangshan fault primarily occur within Devonian formations, including the Xinghongpu Formation (D_3x), Gudaoling Formation (D_{2-3g}), Dafenggou Formation (D_2d), and Xichahe Formation (D_2x). In contrast, the Wangzhuang gold deposit was found within the Upper Devonian–Lower Carboniferous Tieshan Formation (D_3C_1t), which used to be considered a barren formation in this region (Figure 2A). The predominant lithologies hosting mineralization include calcareous (carbonaceous) phyllite and quartz sandstone, and the wall rock is mainly carbonate rock, forming an interstratified rock of carbonate rock and fine clastic rock, which plays a crucial role as a physicochemical interface in ore formation [36,37].

The Wangzhuang gold deposit is located at the northwest end of the Shadonggou anticline of the Nanyangshan synclinorium, while the other NW-trending Songjiayuan fault (F1) and Gangoutai–Qinggou fault (F12) cut through the fold hinge of Shadonggou, and can extend to the mining area in the northwest direction (Figures 2 and 3). The combination of fold and fault constitutes a promising tectonic pattern for ore formation.

Additionally, the Au-Hg-Sb-W anomaly zone in the area is controlled by the Nanyangshan fault, which intersects with the arc-shaped tectonic belt composed of Wangzhuang and Xiaoho gold deposits. The lithology and structure of these ore-bearing strata exhibit certain similarities, thus creating favorable conditions for mineralization. Gold mineralization in this area is closely associated with fault structures, and most of the faults related to mineralization exhibit the characteristics of multi-stage activity following extension and compression. The distribution of gold deposits is controlled by NE-trending main faults and interlayer fracture zones (Figure 2). Gold ore bodies are predominantly found near east–west secondary structural fracture zones, where expansion, contraction, and pinch-out phenomena have been frequently observed.

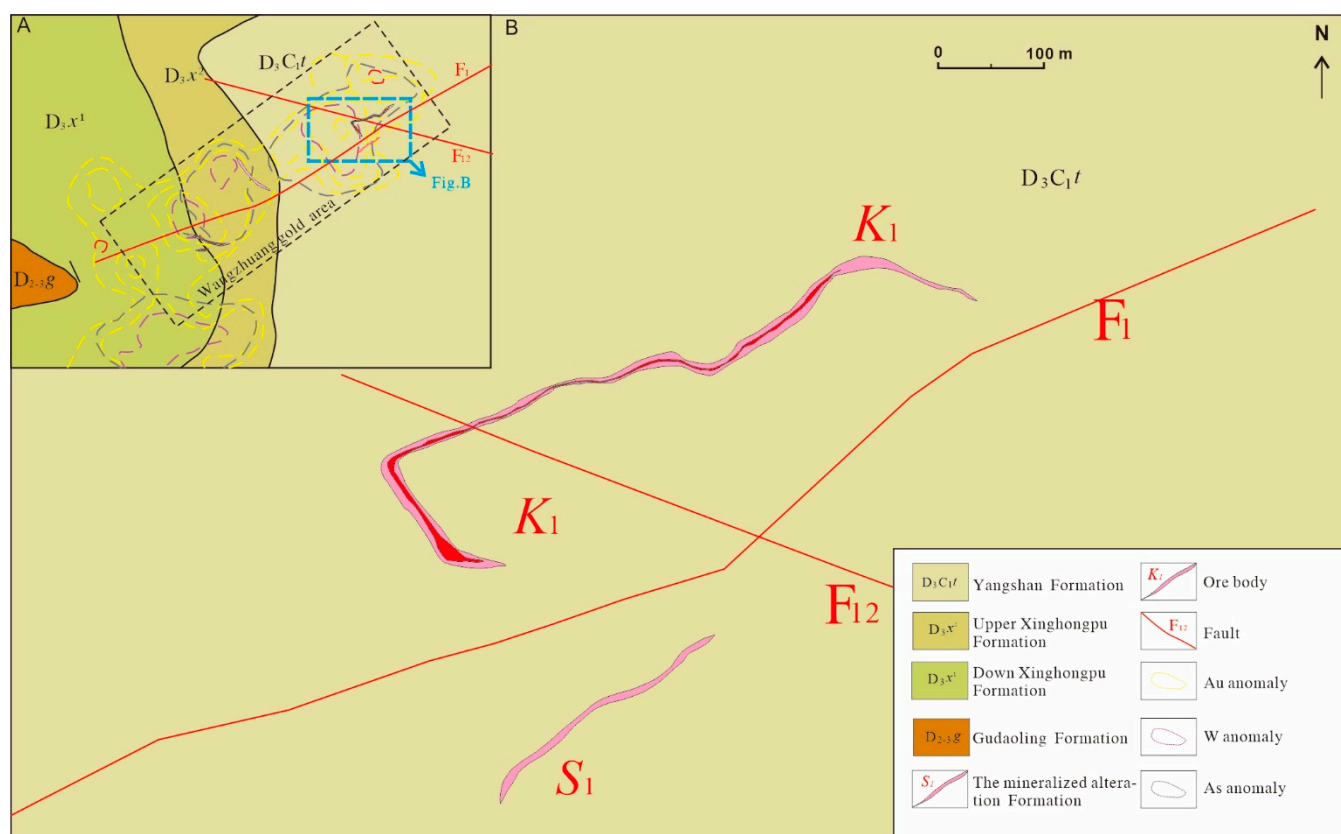


Figure 3. (A) Simplified geologic map of the Wangzhuang gold deposit; (B) eastern exploration area.

The main stratum outcrops in the mining area are the Upper Devonian–Lower Carboniferous Tieshan Formation (D_3C_1t) and Upper Devonian Xinghongpu Formation (D_3x). The orebodies are predominantly hosted in the Tieshan formation along the western axis of the Shadonggou anticline (Figure 3). Stream sediment survey revealed significant and superimposed Au and As anomalies, indicating promising prospects for Au. The Wangzhuang gold deposit is divided into two ore-forming sections. In the eastern ore-forming section, the mineralized bodies primarily occur within the interlayer fracture zone, which is controlled by the interface between limestone and phyllite. Based on current exploration engineering controls, two ore bodies have been found: K_1 as an exposed surface ore body and M_1 as a blind ore body. K_1 extends about 480 m on the surface (Figure 3), with an average grade of 1.41 g/t and an average thickness of 1.3 m. M_1 has an average grade of 1.51 g/t and an average thickness of 5.45 m. The two ore bodies show gently undulating waves along the stratiform fracture zone.

1:50,000 stream sediment surveys within the central ZXB show Cr-Ni-Ti-Co-Mo and W anomalies in the western region, W-Au anomalies in the central region, and Hg-Sb-Au anomalies in the eastern region (Figure 2B). Notably, the presence of the Cr-Ni-Ti-Co-

Mo anomaly suggests potential concealed plutons under the area, which are probably genetically related to the Au-Hg-Sb deposit.

3.2. Ore Texture and Structure

According to the degree of oxidation, the ores in the Wangzhuang gold deposit can be classified into primary and oxidized ores. The oxidized ore typically exhibits a yellowish-brown color and is found within a depth range of 0–30 m from the surface. It commonly contains limonite and iron carbonates as dominant minerals (Figure 4A,C,D). On the other hand, the primary ore comprises cataclastic calcareous (carbonaceous) phyllite-type ore with arsenopyrite (Figure 4B,E), quartz–sulfide-type ore (Figure 4E,F,H,I), and pyrite–sericite–quartzite-type ore (Figure 4E,G), cataclastic calcareous (carbonaceous) phyllite-type ore is the main type.



Figure 4. Field photographs showing alteration characteristics of the surface ore body (A–D) and drill core (E–I) in the Wangzhuang deposit. (A) calcareous (carbonaceous) phyllite and calcarenite with interbedded ore bodies are cut through by late quartz veins; (B) acicular arsenopyrite in calcareous (carbonaceous) phyllite ore bodies; (C) the calcareous (carbonaceous) phyllite ore body develops along the bedding hydrothermal quartz veins, and the arsenopyrite mineralization and enrichment can be seen at the edge of the quartz veins; (D) the multi-layer mineralized body and sand–clastic limestone are interbedded, and the mineralized quartz veins are enriched in the later period and cut through the earlier mineralized alteration zone; (E) two kinds of ore bodies are developed, one is arsenopyrite-phyllite-type, the second is hydrothermal quartz-vein-modified-type; (F–H) the pyrite sericite was altered and developed, and a small amount of arsenopyrite was observed; (I) late quartz calcite veins cut through early ore bodies. Qtz-Quartz; Cal-Calcite; Py-Pyrite; Apy-Arsenopyrite.

3.3. Mineral Textures

The main sulfides in the Wangzhuang gold deposit are pyrite and arsenopyrite. The microstructure analysis reveals that both pyrite and arsenopyrite display multi-stage growth characteristics with textural and morphological differences and can be divided into the following generations:

Py1, Py2: the formation of Py1 primarily occurred particularly in arenaceous limestone and calcareous (carbonaceous) sedimentary rocks during their formation. It generally occurs as strawberry or colloidal aggregates, exhibiting an irregular shape with small particles less than 5 μm (Figure 5A,I). Additionally, many organic-containing pyrite aggregates are observed within this stage. During regional epimetamorphism, pyrite underwent recrystallization and was transformed into cube-like Py2 (Figure 5I).

Apy1a, apy1b: at this stage, a significant influx of hydrothermal solution containing arsenic led to the formation of abundant Apy1a as elongated columns, needles, and large particles (Figure 5C–E,H). Under reflected light, it exhibits a yellow-white gloss. Due to subsequent tectonic processes, the arsenopyrite shows curved or fractured characteristics (Figure 5D,H). It was replaced or filled by later arsenopyrite or pyrite (Figure 5C,D,G). Apy1b occurs mainly as short columns with occasional needle-like structures interspersed among earlier-formed Apy1a crystals. It is comparatively whiter than that observed for Apy1a under reflection microscopy (Figure 5D,E). Notably, fine-grained arsenopyrite with small particles is observed growing around Py2 (Figure 5L).

Py3: the pyrite at this stage exhibits a complex structure, characterized by the presence of arsenian pyrite. It is primarily colloidal, with star-shaped and ring-shaped textures (Figure 5C,D,F–H,J–L). It can be observed that Py3 has replaced the early-formed arsenopyrite (Figure 5C,J), with Py3 being enveloped in a ring shape around Py2 (Figure 5J–L). Similarly, the early arsenopyrite was surrounded by py3 (Figure 5L). Additionally, a small amount of galena and chalcopyrite formed simultaneously with py3, mainly located around the rims of the pyrite and arsenopyrite (Figure 5F,H).

Py4: in the late stage, anhedral pyrite (Py4) replaced early arsenopyrite and formed a ring-shaped structure around arsenic-bearing pyrite (Figure 5J,K). At this stage, the brightness of Py4 under BSE is lower than that of Py3, indicating that the contents of arsenic in Py4 are significantly reduced. The predominant structure observed in Py4 is characterized by anhedral grains arranged in a ring shape (Figure 5J,K).

3.4. Periods and Stages of Mineralization

According to the macro and micro characteristics of the minerals, the ore-forming process of the Wangzhuang gold deposit can be divided into three periods: (1) sedimentary diagenesis; (2) metamorphic period, which is characterized by low-sulfide quartz and is characterized by euhedral, subhedral pyrite, and fine veins of quartz injected parallel to the strata (Figure 4E,G). In this period, the pyrite is arsenic-free (Figure 5I–K); (3) Syn-gold hydrothermal mineralization; (4) post-gold supergene. Based on the variations of the mineralized body, mineral association, and intergrowth relationship, the hydrothermal mineralization period can be further divided into three distinct stages (Figure 6).

1. Stage I is marked by arsenopyrite–arsenian pyrite–quartz assemblage and is characterized by strongly silicified zones of reticulated quartz, disseminated or fine veins arsenopyrite, stellate, and colloidal pyrite (Figure 4B,E,I). Arsenopyrite occurs as needles and columns, and accumulates at broken calcareous slate or the edge of quartz veins (Figure 5D,H). Arsenian pyrite and arsenopyrite show paragenesis, and little galena and chalcopyrite are observed (Figure 5F). Arsenopyrite and arsenian pyrite are the main carriers of gold. This stage shows the most intense mineralization alteration with the highest ore grades.
2. Stage II is marked by low-sulfide quartz assemblage and is characterized by large quartz veins cutting through the ore body or fine veins of quartz (Figure 4A,D). Metal sulfides are enriched at the edge of the quartz vein, while the interior is relatively pure. At this stage, pyrite has a low arsenic content, and the ores have low gold grades.

3. Stage III is marked by calcite–quartz assemblage, and is characterized by a large number of calcite veins. These veins cut through the formation and earlier veins, and are relatively pure, without metal sulfides (Figure 4I).

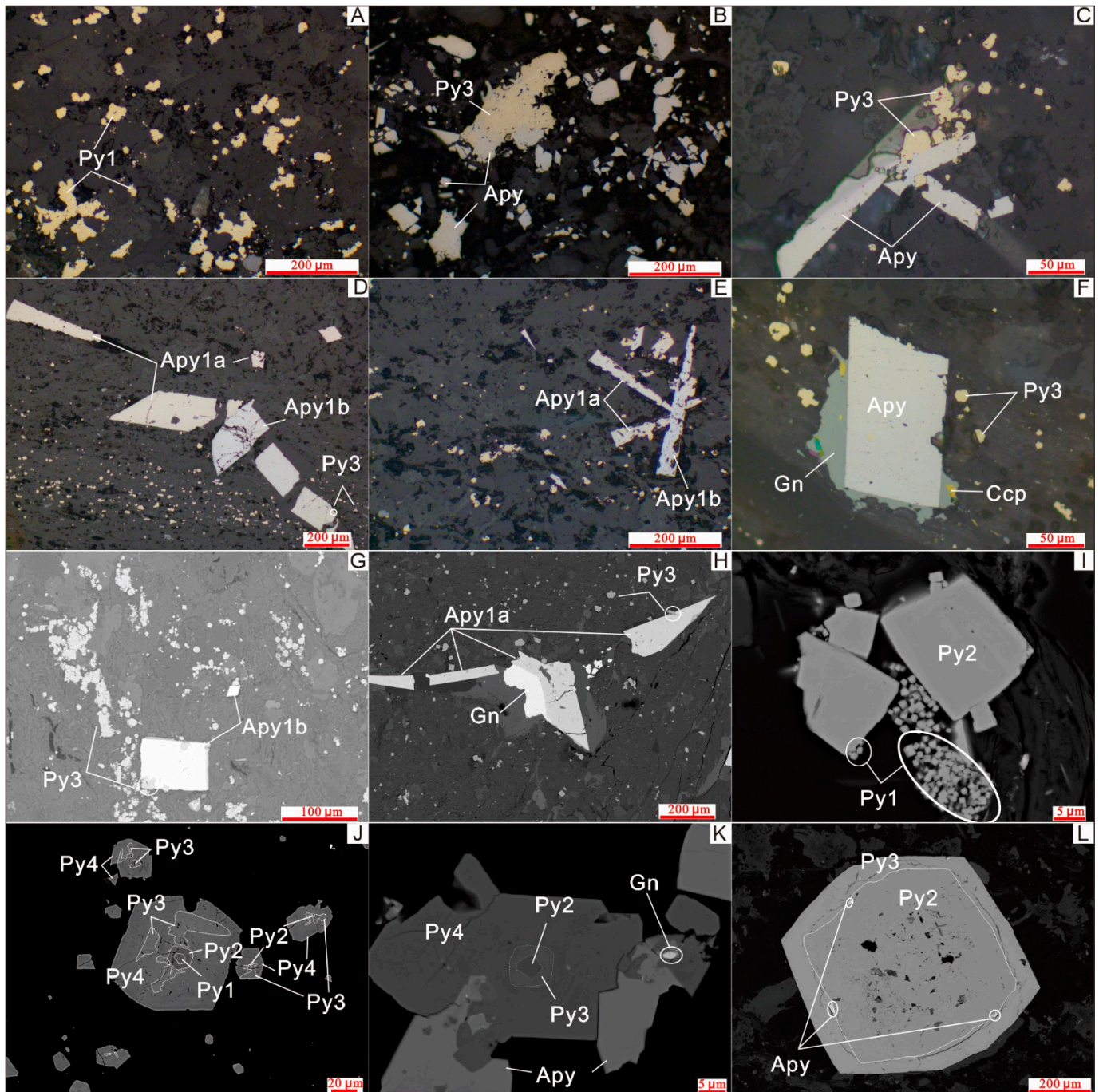


Figure 5. Photomicrographs showing the mineral textures of sulfides in the Wangzhuang gold deposit ((A–F) reflected light; (G–L) BSE images). Py1, strawberry pyrite; Py2, pre-mineralization recrystallized pyrite; Py3, pyrite from main mineralization period; Py4, post-mineralization pyrite; Apy, arsenopyrite; Apy1a, brittle and dislocated needle columnar arsenopyrite of the main mineralization stage; Apy1b, later-stage short columnar arsenopyrite; Gn, galena; Ccp, chalcopyrite.

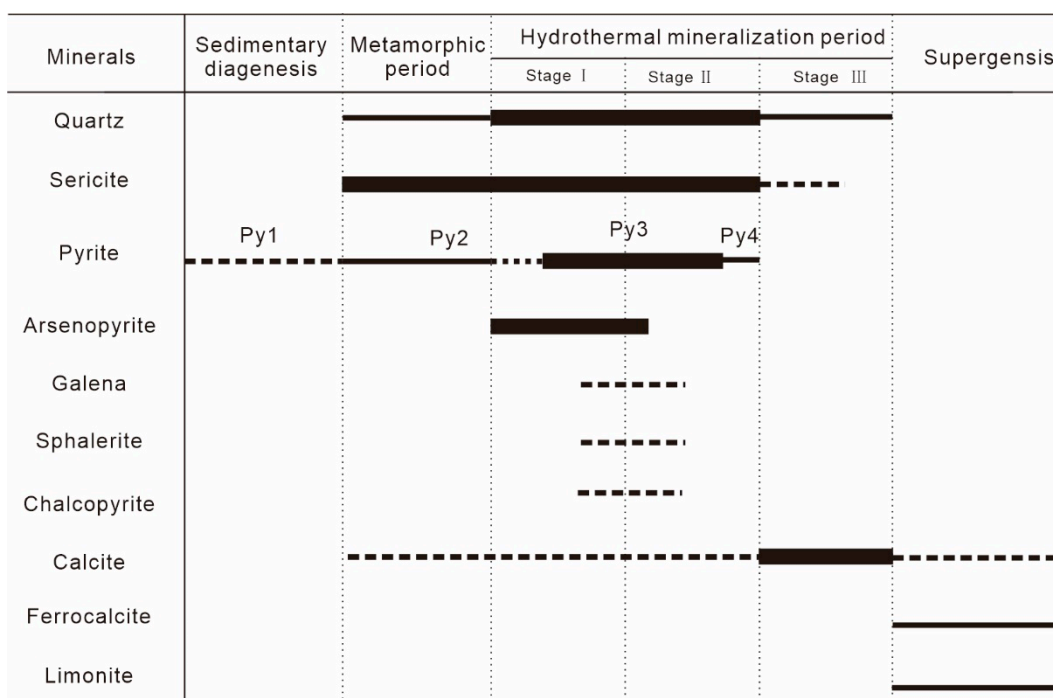


Figure 6. Paragenetic sequence of main minerals from the periods and stages of mineralization. The width of the lines corresponds to the relative abundance of minerals in each stage.

The mineralized bodies, Au grades are strongly positively correlated with the contents of arsenopyrite and arsenian pyrite, as evidenced by the comprehensive analysis of drill samples.

4. Samples and Analytical Methods

More than 30 samples from each stage of mineralization were collected and identified under the microscope. Compositions of pyrite and arsenopyrite with different characteristics at each stage were determined using electron probe microanalysis (EPMA). Their trace elements and S isotopic compositions were further constrained using LA-(MC) ICP-MS.

4.1. Electron Probe Microanalysis

The EPMA of metal sulfides was carried out at the Key Laboratory of Western China’s Mineral Resources and Geological Engineering, Chang’an University. The instrument was a JEOL JXA-8100 electron probe (JEOL, Tokyo, Japan) operated at 20 KV, beam spot current 1×10^{-8} A, beam spot diameter 1 μ m, peak counting time 20 s, and background counting time 10 s. Laboratory standard samples of pyrite, chalcopyrite, galena, sphalerite, bismuth selenide, antimony telluride, and elementary gold, nickel, cobalt, and chromium were used during the analysis. The lower limit of detection of all elements is 0.01%, the relative error of analysis is within $\pm 2\%$, and the test accuracy is 0.01%. All data are ZAF basic corrections.

4.2. In Situ Trace Elements Analysis of Pyrite and Arsenopyrite

In situ trace element analysis of pyrite and arsenopyrite was completed at the State Key Laboratory of Continental Dynamics, Northwest University, Xi’an, China. The analytical instrument was a New wave (esi) dual-wavelength femtosecond LA system (206 and 257 nm) attached to an ICP-MS (Jena PQ-MS Elite). The laser energy was 1 J/cm² and the denudation frequency was 10 Hz. The laser single-point strip etching diameter was 53 μ m, the ablation time was 50 s, the background collection time was 30 s, and the sample collection time was 50 s. Helium gas was used as carrier gas and was mixed with argon gas before entering ICP. The helium gas flow rate was 0.5 L/min, and the argon gas flow rate was about 1 L/min. USGS synthetic sulfide standard MASS-1 was used as the external

standard, Fe element was used as the internal standard, and SRM 610 was used as the monitoring standard [38,39]. The offline data were calculated by ICPMSData Cal software (10.8) [39].

4.3. In Situ S Isotope Analysis of Sulfides

In situ S isotopic composition analysis of pyrite and arsenopyrite was completed at the State Key Laboratory of Continental Dynamics, Northwest University, Xi'an, China. The nanoscale excimer laser ablation system (RESOLUTION M-50, asi) consists of a 193 nm Ar F excimer laser, an X-Y sample moving table, a positioning system, and a two-compartment sample chamber. The energy density of the laser was 3.7 J/cm², the diameter of the spot beam was 37 μm, the laser frequency was 3 Hz, and its carrier gas was high-purity helium with a flow rate of 280 mL/min. A Nu Plasma 1700 Plasma Mass spectrometer, which mainly consists of a Faraday cup and an ion counter, was applied. Faraday cup H5, Ax, and L4 receive ³⁴S, ³³S, and ³²S respectively. To monitor the accuracy of data, a pair of laboratory standards were inserted in every 3 samples. An in-house pyrite standard (NWU-Py-4) was used as an external standard and a pair of sphalerite grains (NBS123/PSPT-3) were used as quality control standards. The mean $\delta^{34}\text{S}_{\text{V-CDT}}$ value of PSPT-3 measured during the analysis was $26.7 \pm 0.2\text{‰}$ (2 S.D., $n = 11$), which is within the error of the reference values reported by Bao [40] and Chen [41] ($\delta^{34}\text{S}_{\text{V-CDT}} = 26.4 \pm 0.2\text{‰}$, 2 S.D.).

5. Results

5.1. Textures and Compositions of Pyrite and Arsenopyrite

As mentioned above, the Wangzhuang gold deposit underwent four hydrothermal stages during its formation, with five sub-stages of sulfides. The Py1 and Py2 contain negligible levels of As (0.03% to 0.11%) and no Au, but showed relatively high contents of S (53.41% to 54.69%). The Apy showed obvious enrichment of Au via EPMA mapping (Figure 7), with Au contents ranging from 0.02% to 0.25%. The Py3 is relatively rich in As (1.35% to 10.38%) and Au (0.05% to 0.20%). Py4 has low As contents, ranging from 0.04% to 0.58%, which is higher than Py1 and Py2 but lower than Py3. Additionally, Py4 can detect Au with lesser contents than 0.07% (Tables 1 and S1). In summary, the highest Au contents were found in Apy, followed by Py3 and Py4.

Table 1. EPMA compositions of the pyrite and arsenopyrite from the Wangzhuang gold deposit (wt%).

Mineral	Period	Au	S	As	Fe	Total
Py4	Post-metallogenic stage	bdl–0.07	52.83–53.49	0.04–0.58	44.73–46.03	98.96–100.18
Py3	Main metallogenic stage	bdl–0.2	45.21–53.64	1.35–10.38	43.18–45.56	98.77–100.66
Apy	Main metallogenic stage	0.02–0.25	21.17–26.13	36.41–43.26	34.81–36.84	98.87–100.64
Py2	Pre-metallogenic stage	bdl	53.41–54.33	0.01–0.11	44.23–45.88	98.55–100.49
Py1	Pre-metallogenic stage	bdl	54.46–54.69	bdl–0.01	46.10–46.21	100.71–101.25

Note: bdl—below the detection limit.

5.2. In Situ Trace Element Compositions of the Sulfides by LA-ICP-MS

Due to Py1's aggregation with more internal impurities, the reliability of trace elements is compromised, and Py4 exhibits a small ring band, rendering it unsuitable for LA-ICP-MS testing (Figure 5A,I–K). Therefore, the focus of this study is primarily on Py2, Py3, and Apy, with Py2 occurring in the pre-mineralization period and Py3, Apy occurring in the main mineralization period. The results indicate that Py2 has low a gold content (ranging from 0.18 to 7.22 ppm), while both Py3 and Apy stages exhibit higher gold contents (ranging from 120 to 915 ppm). The transitional stage Py3-1 has an intermediate gold content, with a range of 22.9 to 60.0 ppm (Figure 8 and Table 2). Furthermore, the contents of Au, W, Pb, Zn, and Sb in Py2 are relatively low, while the contents of Apy, Py3-1, and Py3-2 are relatively high. These results suggest a close relationship between the trace elements Au, W, Pb, Zn, and Sb. In contrast, Co, Cu, and Bi have relatively high contents in Py2, with a

sudden decrease in the Apy stage and a gradual rise in Py3-1 and Py3-2 stages, indicating a weak correlation between Au and Co, Cu, and Bi (Figure 9 and Table 2).

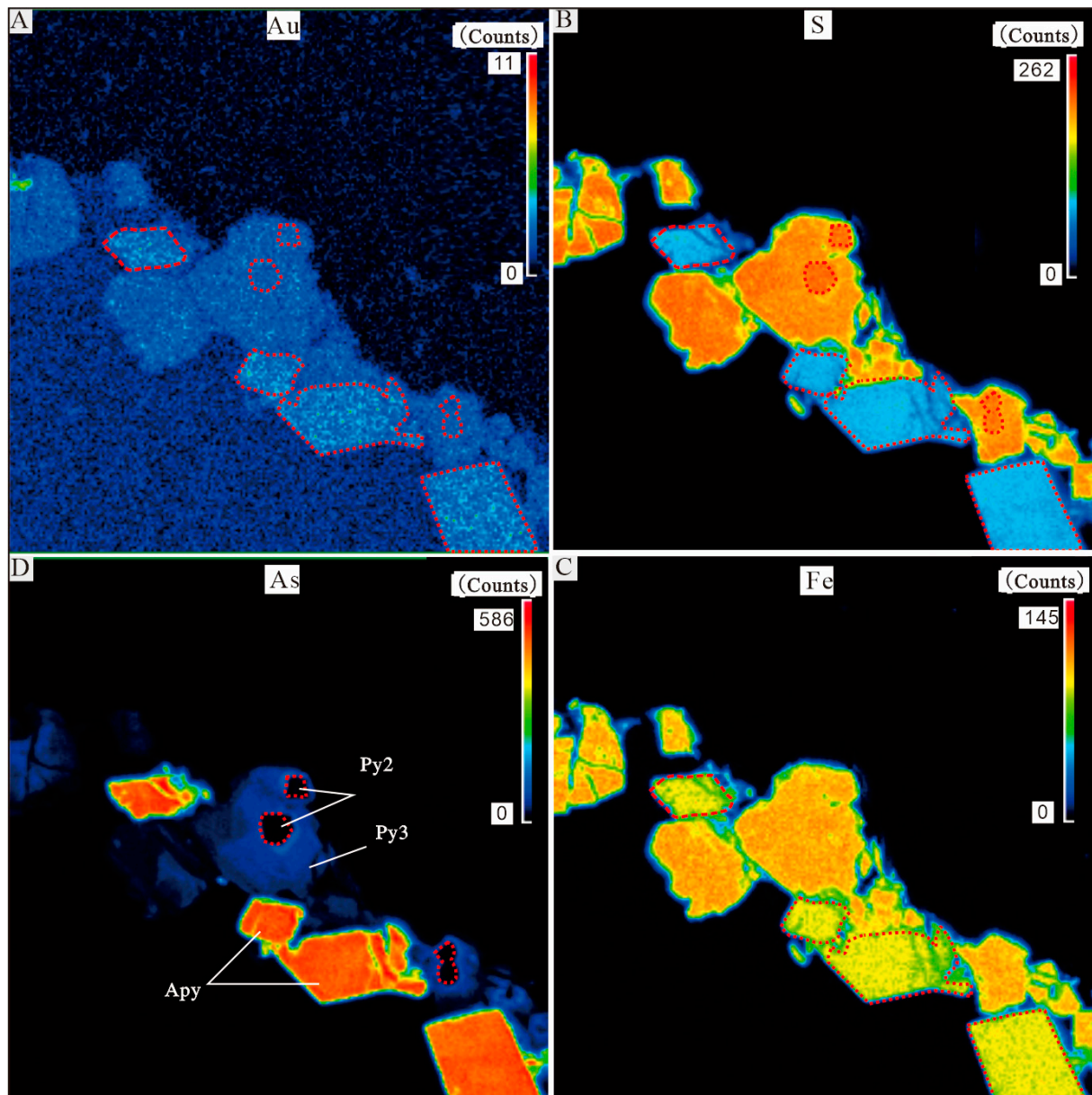


Figure 7. EPMA mapping of Au (A), S (B), As (C), and Fe (D) elements showing the element zoning of the pyrite and arsenopyrite from the Wangzhuang deposit. Py2, pre-mineralization recrystallized pyrite; Py3, pyrite from main mineralization period; Apy, arsenopyrite.

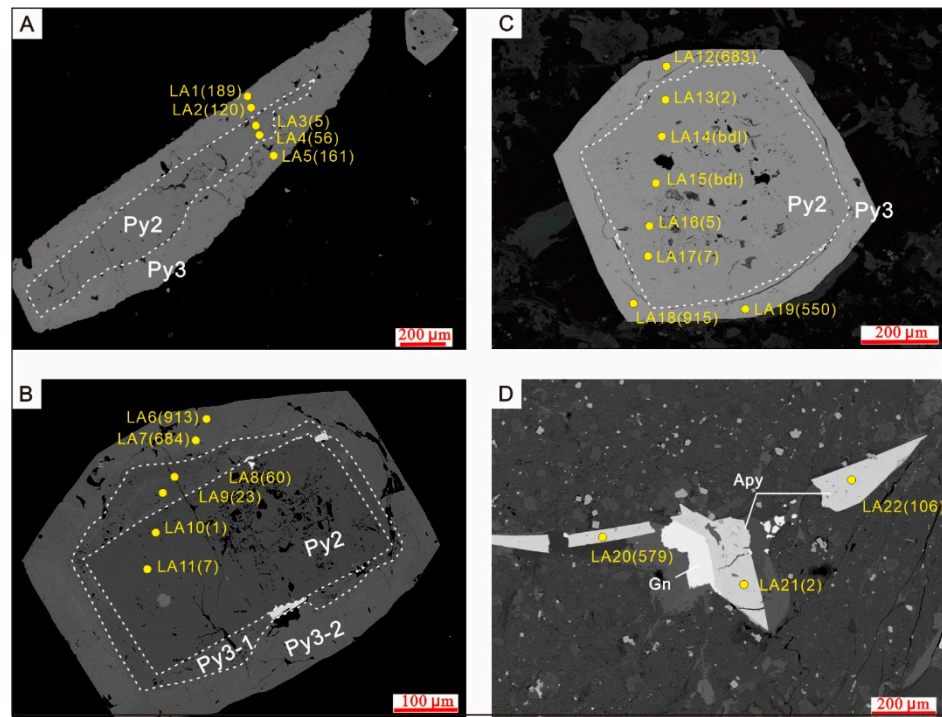


Figure 8. (A–C) Py2 (BSE) is rimmed by Py3, which has similar morphology and relief. (D) Dislocation of arsenopyrite by tectonic event. Yellow dots indicate locations of LA-ICP-MS analysis, and analysis numbers and Au concentration in ppm are shown. Py2 = pre-mineralization pyrite 2; Py3 = main mineralization 3, which contains more As than Py2; Apy= arsenopyrite; Py3-1= earlier-stage pyrite in Py3 with growth zonation.

Table 2. LA-ICP-MS analyses of pyrites in Wangzhuang gold deposit (ppm).

Type	Au	Co	Ni	Cu	Zn	Se	Ag	Sb	W	Tl	Bi	Pb
py3-2	188	64.6	242	151	2.24	16	0.58	29.4	0.98	bdl	5.02	36
	120	26.1	127	137	2.84	bdl	0.1	26.7	1.63	0.09	3.86	93
	160	323	1451	101	2.76	48.7	bdl	14.6	4.54	bdl	1.99	31.3
	913	238	3515	643	2.06	59.3	1.18	190	0.23	0.07	13.3	292
	684	165	2324	599	2.57	5.03	1.01	419	0.92	0.02	19.4	58
	683	451	2939	349	3.76	49.2	0.39	78.9	8.17	0.09	14.7	954
	915	18.7	100	545	3.35	3.6	0.32	77.6	0.43	0.11	12.4	311
	550	373	1984	176	3.08	12.5	0.21	60.9	5.45	bdl	10.5	70.6
py3-1	60	279	1235	255	3.7	0.32	2.27	312	15.3	0.06	32.1	2347
	22.9	249	2097	198	3.11	bdl	1.41	301	4.43	0.07	19.5	589
apy	578	72.1	423	44.1	3.8	37.6	0.07	100	7.87	0.18	0.18	232
	2.17	1174	4703	17.3	0.14	1.12	0.55	745	4.06	0.16	0.72	81.7
	105	51	754	43.7	398	bdl	bdl	379	5.64	0.03	1.61	305
py2	4.85	121	919	52.8	2.39	bdl	0.56	123	0.38	0.09	11.7	200
	55.7	318	2041	75.5	4.33	bdl	0.44	145	4.02	0.31	20.2	263
	1.2	571	149	33.5	9.72	52.7	0.59	29.5	0.08	0.08	132	176
	7.22	438	364	28.7	4.04	bdl	0.65	185	0.64	0.07	29.9	343
	1.79	660	2559	247	3.89	30.2	0.47	48.8	0.14	bdl	22.2	124
	bdl	670	332	37.4	14.1	bdl	0.47	1.96	0.09	0.14	79.1	153
	0.18	5416	1927	32	2.2	bdl	0.5	13	0.07	bdl	7.8	36.5
	5.14	2852	3654	24.2	1.87	bdl	0.42	175	1.3	bdl	29.7	331
	6.91	891	196	39.2	7.2	33.9	0.32	8.11	2.39	0.16	51.1	128

Note: bdl—below the detection limit.

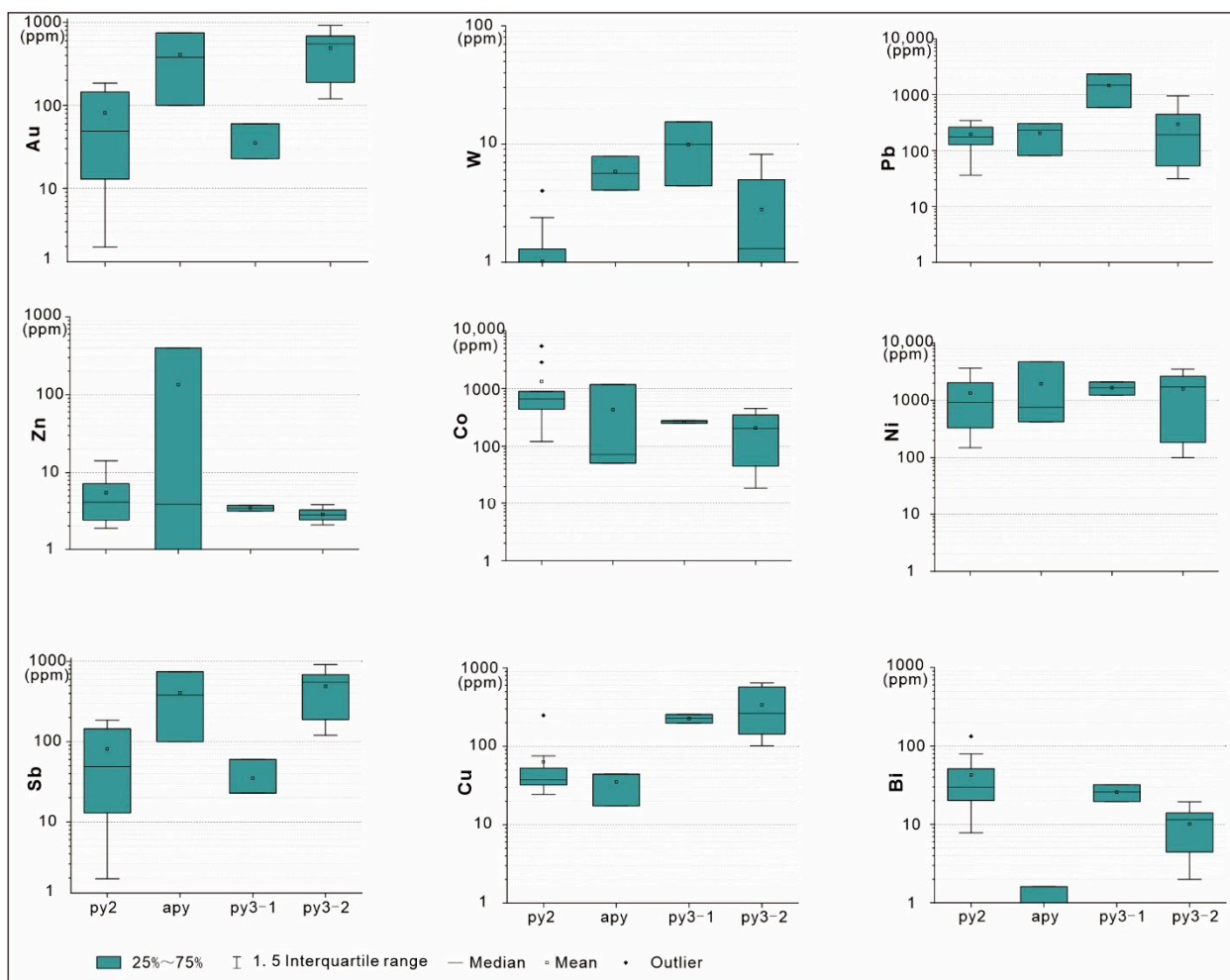


Figure 9. Box-and-whisker diagrams showing LA-ICP-MAS data of Au, W, Pb, Zn, Co, Ni, Sb, Cu, and Bi in Py2, Apy, Py3-1, and Py3-2 from Wangzhuang gold deposit. Py2 = pyrite 2, Apy = arsenopyrite, Py3-1 = pyrite 3-1, Py3-2 = pyrite 3-2.

5.3. S Isotopic Compositions

To investigate the S isotopic compositions of metal sulfides (pyrite and arsenopyrite) at different stages, an LA-MC-ICP-MS in situ S isotope analysis of sulfides from orebodies, alteration zones, and wall rocks was conducted. The $\delta^{34}\text{S}$ values reveal significant variations among metal sulfides at different stages: the $\delta^{34}\text{S}$ values range from 15.3 to 31.2 for Py1 and Py2 during the pre-mineralization stage, 8.4 to 10.9 for Py3 and Apy during the main mineralization stage, and 0.3 to 5.3 for Py4 during the post-mineralization stage (Figure 10, Tables 3 and S2). The results of the in situ S isotopic analysis indicate that there is a significant decrease in $\delta^{34}\text{S}$ values from the pre-mineralization stage to the post-mineralization stage. In particular, there was a sudden change in $\delta^{34}\text{S}$ values from the pre-mineralization to the main mineralization stages, which suggests that the hydrothermal conditions during the main mineralization period were different from those during the pre-mineralization stage. These findings provide important information on the metallogenic processes of pyrite and arsenopyrite in the study area.

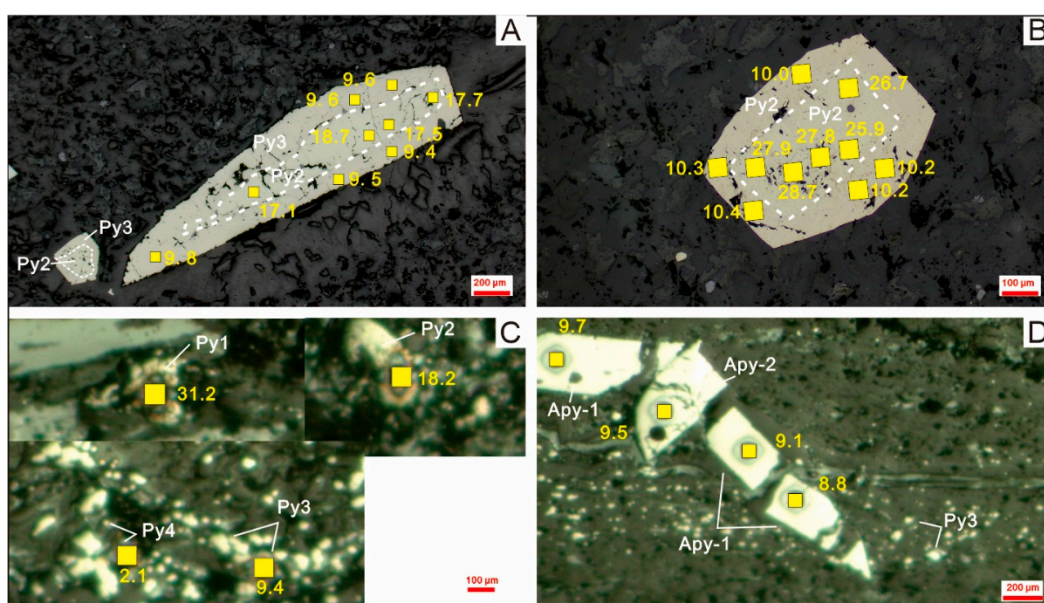


Figure 10. S isotopic values distribution on pyrite (A–C), and arsenopyrite (D) as microscope reflected light images (The yellow squares represent the dot positions). Py1 = pyrite 1; Py2 = pyrite 2; Py3 = pyrite 3; Apy-1= arsenopyrite 1; Apy-2= arsenopyrite 2.

Table 3. LA-MC-ICP-MS In situ S isotopic compositions of pyrite and arsenopyrite from the Wangzhaung gold deposit.

Pyrite Type	Period	$\delta^{34}\text{S}$ (‰)
Py4	Post-metallogenic stage	0.30–5.3
Py3	Main metallogenic stage	5.5–11.2
Apy	Main metallogenic stage	8.4–10.9
Py2	Pre-metallogenic stage	15.8–28.7
Py1	Pre-metallogenic stage	31.2

6. Discussion

6.1. Growth and Geochemistry of Pyrite and Arsenopyrite

6.1.1. The Growth Belt of Pyrite, Arsenopyrite

The sequence of metal sulfide formation in the Wangzhuang gold deposit can be determined as Py1→Py2→Apy→Py3 (including Apy, PbS)→Py4 based on the optical microscope and EPMA analysis of ore-forming material fabric (Figure 11). After Py2, a distinct alteration in hydrothermal characteristics is observed, characterized by the introduction of ore-bearing hydrothermal fluids enriched with As, W, Pb, Sb, Au, etc. During this stage, a significant abundance of arsenic-containing minerals, predominantly arsenopyrite, is formed. Subsequently, with the crystallization of arsenopyrite, a mineral-rich in arsenic, Py3 containing arsenic began to form. As the consumption of arsenic continued, late-stage Py4 with lower levels of arsenic was produced (Figure 11). According to the girth structure of pyrite and variations in Au, single-particle pyrite can be categorized into three stages: the core (Py1 and Py2), the arsenic-rich growth belt (Apy and Py3), and the arsenic-poor outer growth belt (Py4) (Figure 11). These stages correspond to three phases of hydrothermal activity before, during, and after mineralization.

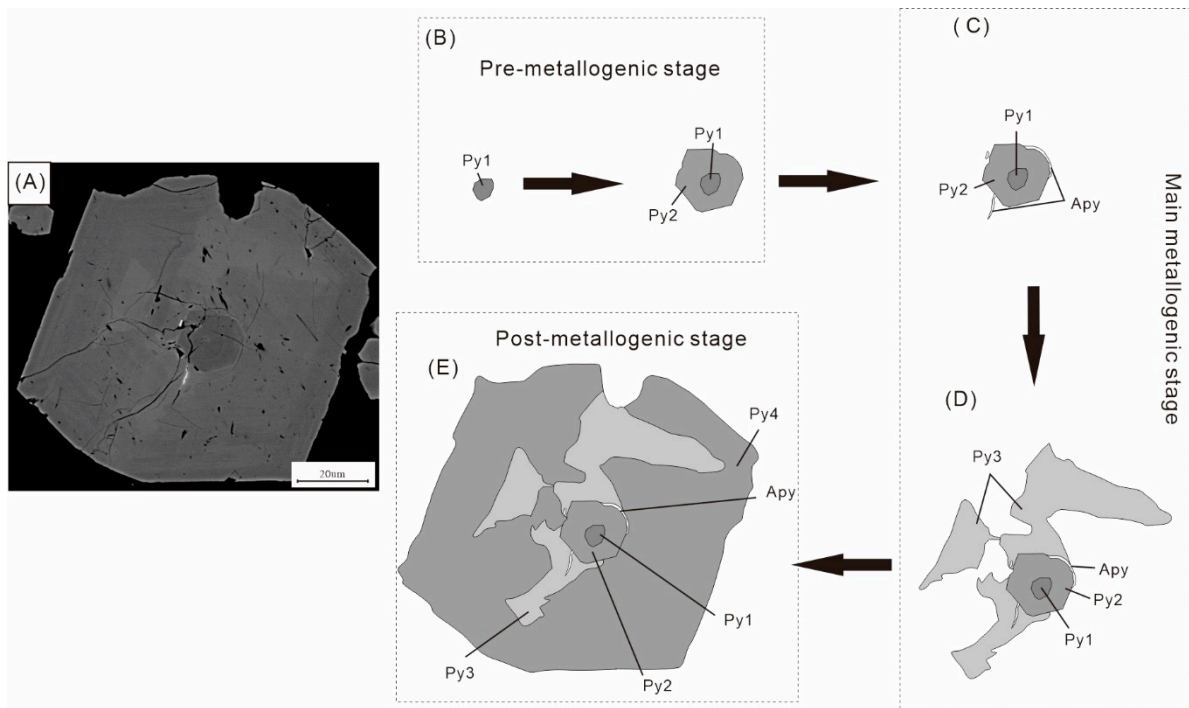


Figure 11. Stages of sulfidic paragenesis. (A) Backscatter electron image of multistage pyrite; (B–E) schematic diagram showing the sequence of formation of the four types of sulfides.

The Co/Ni ratio reflects the genesis of pyrite and arsenopyrite [42–45]. In the studied samples, Co/Ni varied over a narrow range (0.1–4.5), and in 80% of analyses, $10.0 > \text{Co/Ni} > 0.1$, which is typical for hydrothermal pyrite (Figure 12A) [46]. High concentrations of Ni in metallogenic sulfides (Py3 and Apy) may indicate the participation of basic and ultra-basic components supplied into hydrothermal fluids and involved in the deposition of sulfides [44,47], which is consistent with the regional element anomaly (Figure 2B). Additionally, there is a negative correlation between Co/Ni and Au (Figure 12B). Gold is predominantly isomorphous in pyrite with conductivity ($\text{Ni/Co} > 1$), and Co-rich pyrite is not gold-bearing (Figure 11).

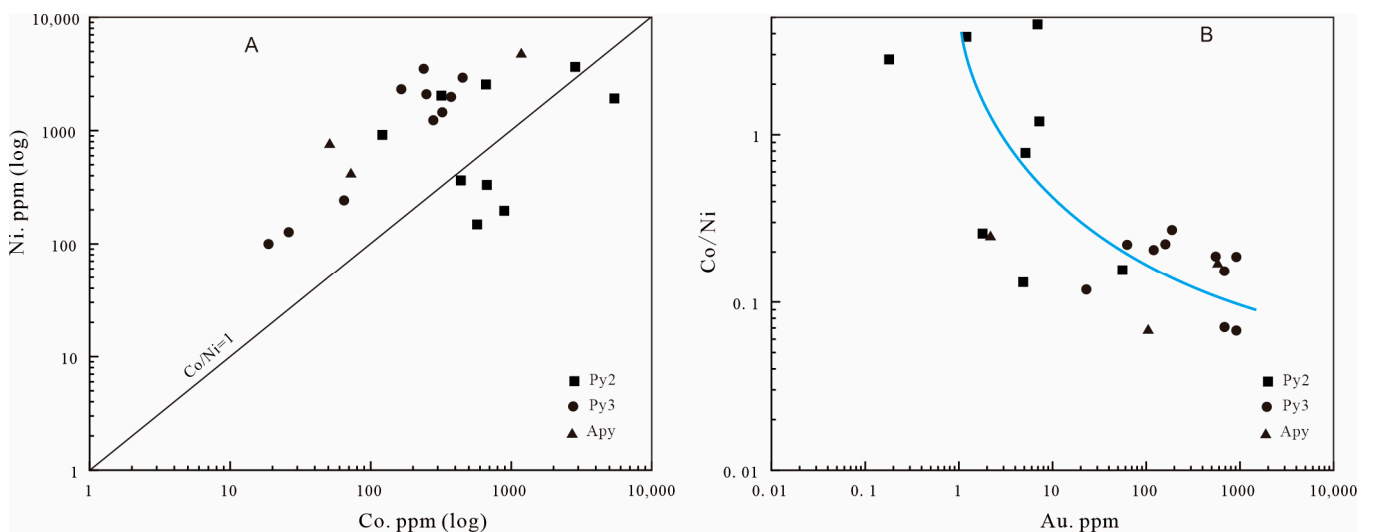


Figure 12. Ratio diagram of Co/Ni (A) and relational diagram of Co/Ni and Au (B).

6.1.2. The Occurrence States of Gold Elements of Pyrite and Arsenopyrite

Previous studies have established a strong correlation between gold (Au) and arsenic (As) in arsenian pyrite [16,48,49], wherein an increase in As substitution within the pyrite structure leads to a higher defect density. This rise in As concentration, attributed to stacking faults or dislocations, serves as the primary mechanism for gold accumulation [50]. Atom probe tomography (APT) has been employed by researchers to investigate arsenian pyrite in Carlin-type gold deposits, revealing the absence of gold nanoclusters and the binding of Au atoms to As atoms in the form of solid solutions [49–51]. While the presence of gold nanoparticles cannot be completely ruled out in previous studies, it can be demonstrated that lattice gold predominates when gold elements are relatively uniformly distributed. The EPMA analysis of the Wangzhuang gold deposit reveals a homogeneous distribution of gold elements, while the LA-ICP-MAS analysis demonstrates relatively consistent Au contents within the arsenian ring belt (Figure 8 and Table 2). Additionally, the As/Au ratio boundary graph (Figure 13) shows that the gold in the pyrite (Py3) during the main mineralization period of Wangzhuang gold deposit is in the state of lattice gold occurrence. Therefore, it can be inferred that the occurrence state of lattice gold predominates in the Wangzhuang gold deposit.

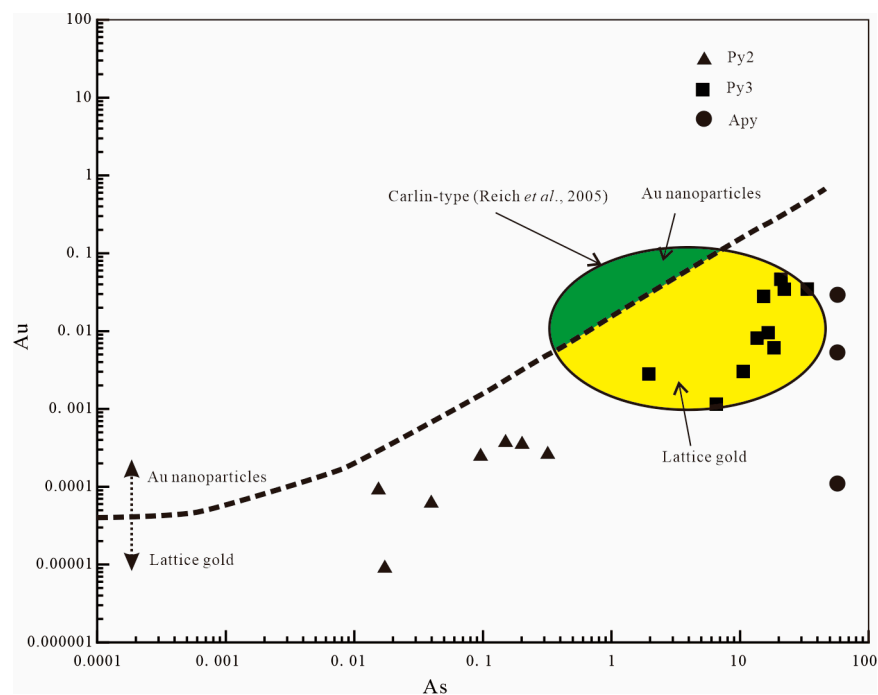


Figure 13. Simplified As/Au ratio boundary graph of Wangzhuang gold deposit. The broken line represents the limit above which Au nanoparticles are meant to form [52], Carlin-type region from Reid [52].

Based on the close correlation between Au and As in pyrite, it is an effective means of studying the activity characteristics of Au by analyzing the substitution of As [53,54]. Previous studies have found that the entry of As into arsenian pyrite may exist in the following forms: As^- replaces S^- in pyrite [55–57]; As^{3+} or As^{2+} instead of Fe^{2+} [53,57,58]; or As mixed in in the form of nanoparticles As^0 [54]. A ternary plot of the arsenian pyrite Fe-S-As (at %) can prove whether As replaces S or Fe [49,53], a trend line parallel to the As-S contents distribution as defined in the Fe-S-As (at%) ternary diagram of Wangzhuang gold deposit, indicating that As replaced S in arsenian pyrite (Figure 14A), and the As and S also showed a strong negative correlation ($R^2 = 0.923$), measured by EPMA, further corroborating this result (Figure 14B).

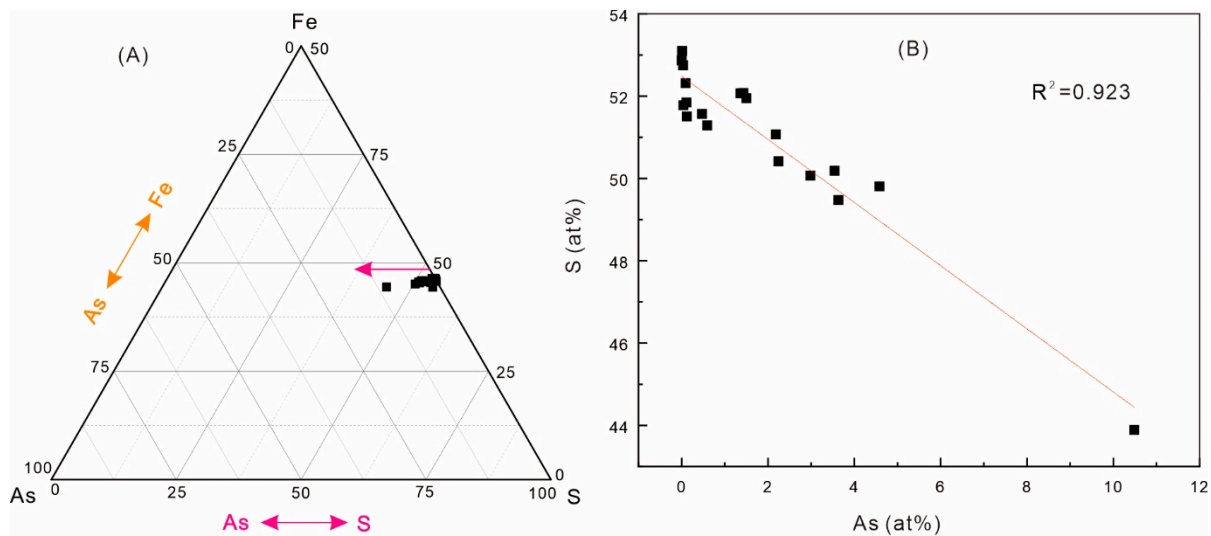


Figure 14. Composition of pyrite on As-Fe-S ternary from analyses in Table S1 (A) and As vs. S for pyrite from Wangzhuang gold deposit (B).

6.1.3. The Source of Ore-Forming Materials Revealed by Trace Elements

It can be seen that the formation of the Wangzhuang gold deposit is closely related to the addition of ore-bearing hydrothermal fluids with different properties. This process resulted in the generation of a significant number of arsenic-containing minerals, where As atoms replaced S atoms within the pyrite lattice, leading to layer faults or dislocations in the crystal structure and facilitating the incorporation of Au into the pyrite lattice. The variations in pyrite composition at different stages indicate significant changes in hydrothermal properties during the mineralization process. The low concentrations of As and Au in stage I (Py1 and Py2) suggest that Au was not significantly enriched during early deformation and metamorphism processes. Stage II (Apy and Py3) exhibits hydrothermal activities characterized by abundant As, Sb, Pb, W, Au, etc. (Figure 9), indicating distinct ore-bearing hydrothermal properties compared to those observed in stage I. These findings imply that the ore-bearing hydrothermal fluid did not originate from the sedimentary strata but from depth.

6.2. Source of Ore-Forming Fluid Revealed by Sulfur Isotope

The S isotopic compositions of the Wangzhuang gold deposit exhibit significant variations from the pre-mineralization to the post-mineralization period. In the pre-mineralization period, the $\delta^{34}\text{S}$ value was predominantly greater than 15‰, with an average $\delta^{34}\text{S}$ value exceeding 20‰. However, during the mineralization period, there is a sudden decline in the $\delta^{34}\text{S}$ value to less than 10‰, gradually decreasing to nearly 0 in post-mineralization stages (Figures 10 and 15A). This evolution can be characterized by two gradient processes (Py1 to Py2 and Py3 (Apy) to Py4), as well as a mutation process from Py2 to Py3. The Xiaohe gold deposit, situated approximately 3 km north of the Wangzhuang Gold deposit (Figure 2A), exhibits similar characteristics in terms of S isotopic variation. Specifically, the $\delta^{34}\text{S}$ values exceed 20 during the pre-mineralization and fall below 20 during mineralization. Furthermore, a decreasing trend in $\delta^{34}\text{S}$ values can be observed in metal sulfides, as per their crystallization sequence. These findings suggest a continuous influx of hydrothermal fluids with low $\delta^{34}\text{S}$ values during mineralization; however, the final $\delta^{34}\text{S}$ values consistently remain above 0‰ [59]. This phenomenon aligns with the decrease in $\delta^{34}\text{S}$ from pre-mineralization to post-mineralization stages in the Wangzhuang gold deposit. Additionally, the Wangzhuang gold deposit exhibits $\delta^{34}\text{S}$ values in the mineralization period that align closely with those of the Jinlongshan Carlin-type gold deposit (Figure 15B). Given that the above gold deposits are controlled by the Nanyangshan fault at a spatial scale, their ore-hosting structures represent fractured zones influenced by sequence

stratigraphic boundaries, while exhibiting comparable similarities in wall rocks. These findings suggest that fluid characteristics within this area's gold deposits remain consistent on a smaller scale, potentially influenced by a shared hydrothermal system.

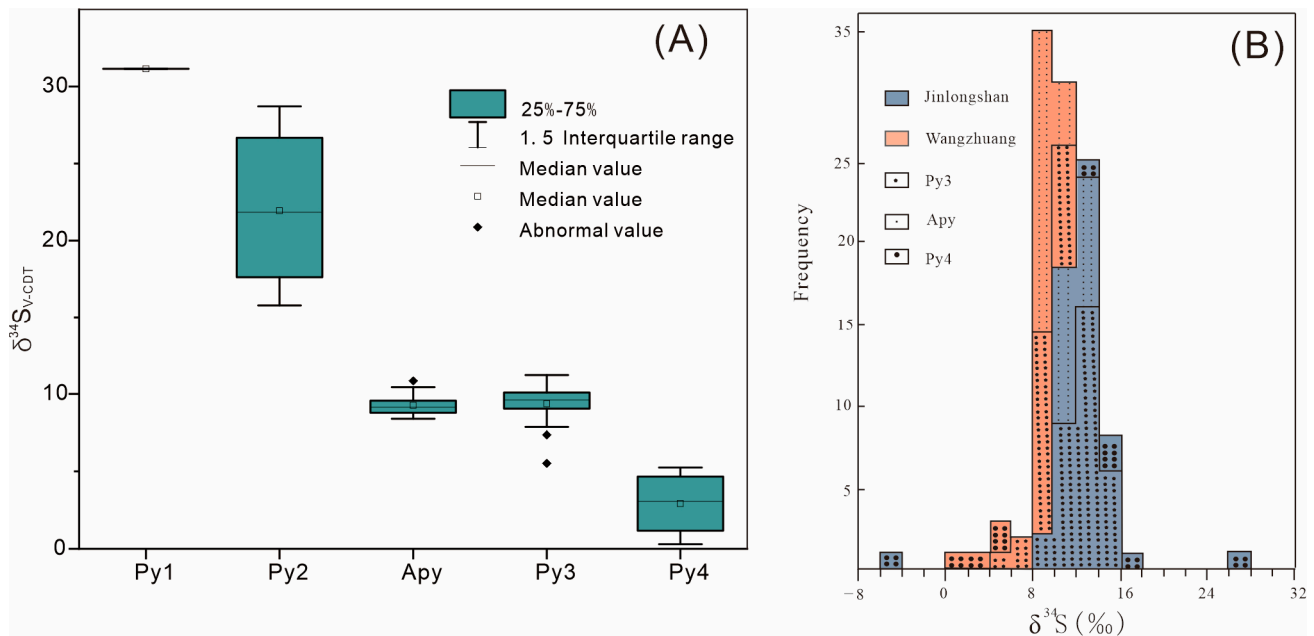


Figure 15. Boxplot diagrams $\delta^{34}\text{S}$ date of pyrite and arsenopyrite in each stage of Wangzhuang gold deposit (A) and histogram of $\delta^{34}\text{S}$ date in ore pyrite from the Wangzhuang (date from this study) and Jinlongshan (date from Ma [29]) (B).

The $\delta^{34}\text{S}$ values of the Py2 stage during pre-mineralization range from 15.8‰ to 28.7‰, while the $\delta^{34}\text{S}$ values without arsenic core range from 21.8 to 28.7 (Tables 3 and S2), exhibiting significantly large positive value, which can be attributed to thermochemical sulfate reduction (TSR) occurring within a closed system [60,61]. Since Py1 was found to be completely modified and exhibited a similar S isotopic composition to Py2, the latter was chosen as the primary focus for investigating the pre-mineralization stage. The pyrite formed during the pre-mineralization transformation of the Jinlongshan gold deposit in the same region also displayed a significantly positive value [20], which is consistent with Wangzhuang and Xiaohe gold deposits in the Zhen'an-Xunyang Basin in terms of regional tectonic evolution, indicating that all these deposits were formed within an enclosed basin environment through regional thermal metamorphism.

The $\delta^{34}\text{S}$ values of the Apy stage during the main mineralization period range from 8.4‰ to 10.9‰, with a more concentrated dataset. As one of the primary gold-bearing minerals, Apy is an important mineral formed in the thermochemical stage of the main mineralization period and occurs earlier than Py3. In combination with its thermochemical properties, it is distinguishable from trace element compositions during pre-mineralization. The $\delta^{34}\text{S}$ values of Py3 during the main mineralization period range from 5.5‰ to 11.2‰ (Tables 3 and S2), exhibiting significant differences compared to pre-mineralization Py1 and Py2 (Figure 15A) and relatively smaller variations when compared to those observed in Apy. These findings suggest that the sulfur present in the hydrothermal solution associated with the ore did not originate from pyrite or organic sulfur decomposition within the wall rocks, nor was it formed through thermochemical sulfate reduction (TSR). Previous studies on gold deposits have demonstrated that fluid-derived sulfur can be attributed to three potential sources: (1) magmatic origin [16]; (2) homogeneous deep crustal metamorphic origin [11,20,62]; and (3) sedimentary origin [63]. The S isotopic characteristics of metal sulfides (Apy and Py3) in the Wangzhuang gold deposit during the metallogenic period

differ from those of metal sulfides (Py1 and Py2) in the sedimentary metamorphic stage; thus, it can be excluded as a potential cause for sedimentary transformation.

The $\delta^{34}\text{S}$ values of pyrite during the post-mineralization stage Py4 range from 0.3‰ to 5.3‰, which are relatively smaller compared to those observed during the main mineralization period. This observation suggests that Py4 is a result of the gradual homogenization of hydrothermal reactions in the early stages and subsequent precipitation of metal sulfides leading to progressive decline in ^{34}S .

The $\delta^{34}\text{S}$ value of pyrite in the Wangzhuang gold deposit exhibits a decreasing trend from the early stage to the late stage throughout the entire mineralization process. Moreover, there is an abrupt change in thermochemical properties, suggesting that this characteristic of thermochemical fluid represents the primary ore-forming fluid, distinct from the metamorphic exudation of ore-bearing strata. Therefore, the origin of this fluid could be either magmatic or deep basement metamorphic. In the Zhen'an-Xunyang Basin, the gold deposits are closely associated with tectonic deformation and metamorphism, with the majority of deposits hosted within secondary structural formations or ore-conducting structures. Hence, it is difficult to determine whether the fluid is of metamorphic or magmatic origin based on its ore-forming materials. Goldfarb [11] concluded that fluid-rock metasomatic reactions occur during the migration process of metamorphic fluids and at the ore-forming site, resulting in overlapping isotopic values from different source areas. However, due to the formation of fluids along fault channels, which dominate the hydrothermal system, significant changes along the fluid path are unlikely. Based on this, the gradual change following fluid mutation is attributed to fluid-rock metasomatic reactions; however, this effect diminishes with fluid migration, aligning more closely with the characteristics of the ore-forming fluid itself. Therefore, $\delta^{34}\text{S}$ values in the middle and late stages of this period are considered to better reflect the true nature of the fluid, and $\delta^{34}\text{S}$ values within this range (0.3‰~5.3‰) may more likely represent magmatic–hydrothermal fluids. Furthermore, combined with the regional element anomaly, which show the anomaly zoning of $W \rightarrow Au (W) \rightarrow Hg, Sb (Au)$ from the west to the east, as well as the deposits' distributions, which change from high temperature to low temperature (Figure 2B). Additionally, there is a comprehensive anomaly of Cr-Ni-Ti-Co-Mo located to the west of Wangzhuang and Xiaohu Gold deposits (Figure 2B), indicating that there is a concealed pluton on the west side of the deposits. The metamorphic fluids tend to homogenize fluid properties and are less likely to generate such extensive elemental zones [11–13]. Conversely, the behavior of magmatic fluids is more influenced by the spatial distribution of intrusions, which aligns better with the occurrence of large-scale elemental zones [64–67]. Consequently, it is inferred that the metallogenic hydrothermal fluid in the middle zone of Zhen'an-Xunyang Basin is predominantly derived from magmatic sources.

6.3. Ore-Forming Process

In recent years, a series of early-to-late Mesozoic plutons have been discovered in the Zhen'an-Xunyang Basin and its surrounding areas. The diagenesis dates primarily range from 150 to 125 Ma [68–72], which align closely with the formation ages of several gold deposits in the region (e.g., Jinlongshan's metallogenic age is 142 Ma and Xiajia-dian's metallogenic age is 139 Ma or 141 Ma) [19,73,74]. Previous studies suggested that Carlin-type gold deposits are predominantly found in tectonic settings characterized by extension or the transition from compression to extension [8,10,20,26,75,76], which is consistent with the extensional tectonic stress field dominant in the Zhen'an-Xunyang Basin and the regional tectonic background of the Yanshanian stage [31]. Meng [77] and Zhang [31] highlighted the connection between the evolution of ZXB during the Late Devonian to Early Carboniferous era and the southern collision of the North Qinling Mountains. This collision led to a shift in ZXB's geological features: from a shallow-water carbonate platform in the Devonian period, it transformed into a rifted basin during the Late Devonian and Early Carboniferous periods due to fault subsidence in the uplifted regions [77]. In addition, Yin [78,79] provided evidence from lithofacies' paleogeography that the south

Qinling region was primarily characterized by a rifted sedimentation. Based on the above conclusions, the formation of the Zhen'an-Xunyang Basin was mainly restricted by the extensional tectonic stress field, and the regional stress was in a state of decompression. During the intrusion of magmatic rocks, ore-forming elements were extracted from the deep basement through gas, water, and hydrothermal fluids. Subsequently, these fluids migrated along the regional deep fault (Nanyangshan fault) under decompressive conditions, and precipitated ore-forming materials within upper secondary tectonic fracture zones. Through thermal convection within the rock mass, ore-bearing hydrothermal fluids continuously interacted with wall rocks to replace and assimilate them, resulting in the gradual homogenization of fluid channels. Later on, due to the differential unloading temperatures of ore-forming materials, varying migration distances led to vertical and horizontal zoning patterns observed in tungsten, gold, and mercury–antimony deposits (Figure 16). Therefore, it is plausible that the hydrothermal tungsten deposits, Carlin-type gold deposits, and medium–low-temperature hydrothermal mercury-antimony deposits are all products of a shared hydrothermal metallogenic system.

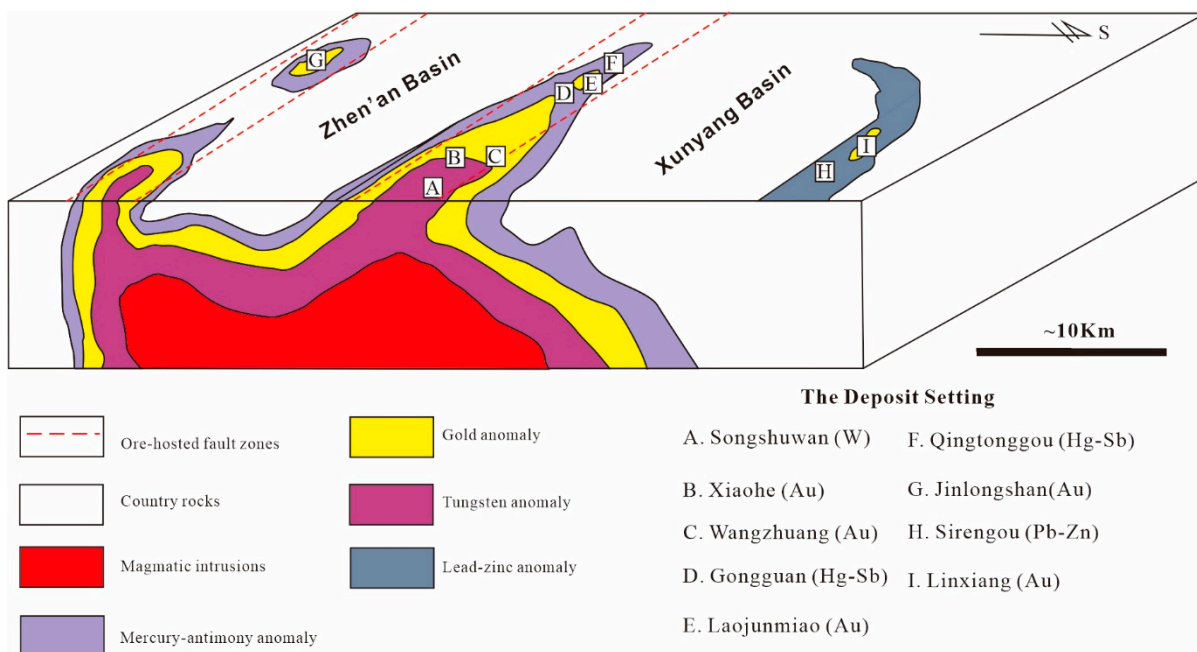


Figure 16. Map of metallogenic regularity in the Zhen'an-Xunyang Basin.

7. Conclusions

1. The hydrothermal mineralization period of the Wangzhuang gold deposit can be divided into four mineralization stages: I, low-sulfide quartz early stage; II, main metallogenic stage of arsenopyrite–arsenian pyrite–quartz; III, low-quartz sulfide stage; IV, late stage of calcite–quartz. Stage II serves as the main phase of mineralization, during which significant amounts of arsenopyrite and arsenian pyrite crystallize. The positive correlation between the abundance of arsenic-bearing minerals and gold grades reveals their genetic link.
2. The metal sulfide generation sequence of the Wangzhuang gold deposit is Py1 → Py2 → Apy → Py3 (Apy, PbS) → Py4. After the formation of Py2, there is a significant presence of fluid rich in As, Sb, Pb, W, and Au. The replacement of S by As atoms in the pyrite lattice resulted in layer faults or dislocations in the crystal structure and contributed to the incorporation of Au into pyrite.
3. The δ³⁴S values of the metal sulfides in the Wangzhuang gold deposit during pre-mineralization, mineralization, and post-mineralization periods range from 15.8‰ to 31.2‰, 5.5‰ to 11.2‰, and 0.3‰ to 5.3‰, respectively. These results suggest that there was a significant hydrothermal interaction between fluids and rocks in the

early stage of mineralization. Furthermore, the $\delta^{34}\text{S}$ values ranging from 0.3‰ to 5.3‰ after the mineralization period imply an injection of magmatic fluid into the Wangzhuang gold deposit during its metallogenic process.

4. The concealed pluton on the west side of the central belt of the basin is probably the main cause for the vertical and horizontal zonation of W, Au, Hg, and Sb deposits.

Supplementary Materials: The following supporting information can be downloaded at: <https://www.mdpi.com/article/10.3390/min13111459/s1>, Table S1: Detailed EPMA compositions of the pyrite and arsenopyrite from the Wangzhuang gold deposit (wt%); Table S2: Detailed LA-MC-ICP-MS In-situ S isotopic compositions of pyrite and ar-senopyrite from the Wangzhuang gold deposit.

Author Contributions: J.L., H.W., Y.G. and L.W. offered advice for this work; W.M., Z.Z., H.W., W.T., B.J., X.Z. and N.L. conducted the field work; W.M. performed the experiments and organized this paper. All authors have read and agreed to the published version of the manuscript.

Funding: This research was funded by this project granted by Natural Science Basic Research Program of Shaanxi (Grant Nos. 2023-JC-QN-0363, 2023-JC-QN-0345), a program of the National Natural Science Foundation of China (Grant Nos. 42272095) and the work items of the China Geological Survey (Grant Nos. DD20230370, DD20211552, DD20230057 and DD20230060).

Data Availability Statement: The authors confirm that the data supporting the findings of this study are available within the article.

Acknowledgments: We are grateful to Zonghui Li and Jiabin Teng of Xi'an Center of China Geological Survey and Xinke Zhao of Shaanxi Geology and Mining First Geological Team Co., LTD. for their enthusiastic help with the field work. Finally, I would like to thank the two reviewers for their valuable comments on the manuscript.

Conflicts of Interest: The authors declare no conflict of interest.

References

1. Kesler, S.E.; Fortuna, J.; Ye, Z.; Alt, J.C.; Core, D.P.; Zohar, P.; Borhauer, J.; Chryssoulis, S.L. Evaluation of the Role of Sulfidation in Deposition of Gold, Screamer Section of the Betze-Post Carlin-Type Deposit, Nevada. *Econ. Geol.* **2003**, *98*, 1137–1157. [[CrossRef](#)]
2. Henry, C.D.; John, D.A.; Leonardson, R.W.; McIntosh, W.C.; Heizler, M.T.; Colgan, J.P.; Watts, K.E. Timing of Rhyolite Intrusion and Carlin-Type Gold Mineralization at the Cortez Hills Carlin-Type Deposit, Nevada, USA. *Econ. Geol.* **2023**, *118*, 57–91. [[CrossRef](#)]
3. Mao, J.; Qiu, Y.; Goldfarb, R.; Zhang, Z.; Garwin, S.; Fengshou, R. Geology, distribution, and classification of gold deposits in the western Qinling belt, central China. *Miner. Depos.* **2002**, *37*, 352–377. [[CrossRef](#)]
4. Chen, Y.; Santosh, M. Triassic tectonics and mineral systems in the Qinling Orogen, central China. *Geol. J.* **2014**, *49*, 338–358. [[CrossRef](#)]
5. Chen, M.; Mao, J.; Li, C.; Zhang, Z.; Dang, Y. Re-Os isochron ages for arsenopyrite from Carlin-like gold deposits in the Yunnan-Guizhou-Guangxi “golden triangle”, southwestern China. *Ore Geol. Rev. J. Compr. Stud. Ore Genes. Ore Explor.* **2015**, *64*, 316–327. [[CrossRef](#)]
6. Liu, J.; Dai, H.; Zhai, D.; Wang, J.; Wang, Y.; Yang, L.; Mao, G.; Liu, X.; Liao, Y.; Yu, C.; et al. Geological and geochemical characteristics and formation mechanisms of the Zhaishang Carlin-like type gold deposit, western Qinling Mountains, China. *Ore Geol. Rev.* **2015**, *64*, 273–298. [[CrossRef](#)]
7. Li, J.; Zhao, X.; Deng, X.; Tan, J.; Hu, H.; Zhang, D.; Li, Z.; Li, H.; Rong, H.; Yang, M.; et al. An overview of the advance on the study of China’s ore deposits during the last seventy years. *Sci. Sin. Terrae* **2019**, *49*, 1720–1771, (In Chinese with English abstract).
8. Liu, J.; Liu, C.; Carranza, E.J.M.; Li, Y.; Mao, Z.; Wang, J.; Wang, Y.; Zhang, J.; Zhai, D.; Zhang, H.; et al. Geological characteristics and ore-forming process of the gold deposits in the western Qinling region, China. *J. Asian Earth Sci.* **2015**, *103*, 40–69. [[CrossRef](#)]
9. Mao, J.W.; Li, X.F.; Li, H.M.; Qu, X.M.; Zhang, C.Q.; Xue, C.J.; Wang, Z.L.; Yu, J.J.; Zhang, Z.H.; Feng, C.Y.; et al. Types and Characteristics of Endogenous Metallic Deposits in Orogenic Belts in China and Their Metallogenic Processes. *Acta Geol. Sin.* **2005**, *79*, 342–372. (In Chinese)
10. Cline, J.S.; Muntean, J.L.; Xuexiang, G.U.; Xia, Y. A Comparison of Carlin-type Gold Deposits: Guizhou Province, Golden Triangle, Southwest China, and Northern Nevada, USA. *Earth Sci. Front.* **2013**, *1*, 1–18.
11. Goldfarb, R.J.; Groves, D.I. Orogenic gold: Common or evolving fluid and metal sources through time. *Lithos* **2015**, *233*, 2–26. [[CrossRef](#)]
12. Groves, D.I.; Goldfarb, R.J.; Gebre-Mariam, M.; Hagemann, S.G.; Robert, F. Orogenic gold deposits: A proposed classification in the context of their crustal distribution and relationship to other gold deposit types. *Ore Geol. Rev.* **1998**, *13*, 7–27. [[CrossRef](#)]

13. Goldfarb, R.J.; Hart, C.; Marsh, E.E. Orogenic gold and evolution of the Cordilleran orogen. In *Ores and Orogenesis: Circum-Pacific Tectonics, Geologic Evolution, and Ore Deposits: Arizona Geological Society Digest*; Arizona Lithographers Inc: Tucson, Arizona, 2008; pp. 311–324.
14. Chen, Y.J.; Zhang, J.; Zhang, F.X.; Franco, P.; Li, C. Carlin and Carlin-like Gold Deposits in Western Qinling Mountains and Their Metallogenic Time, Tectonic Setting and Model. *Geol. Rev.* **2004**, *2*, 134–152. (In Chinese)
15. Chen, M.H.; Guo, S.X.; Xie, X.Y.; Ma, K.Z. Hydrothermal mineralogy of Nibao Carlin-type gold deposit, Guizhou Province and its geological significances. *Miner. Depos.* **2018**, *37*, 502–520. (In Chinese)
16. Xie, Z.; Xia, Y.; Cline, J.C.; Pribil, M.P.; Koenig, A.; Tan, Q.; Wei, D.; Wang, Z.; Yan, J. Magmatic origin for sediment-hosted au deposits, Guizhou Province, China: In situ chemistry and sulfur isotope composition of pyrites, shuiyindong and Jinfeng deposits (Article). *Econ. Geol.* **2018**, *113*, 1627–1652. [\[CrossRef\]](#)
17. Jin, X.; Zhao, J.; Feng, Y.; Hofstra, A.H.; Deng, X.; Zhao, X.; Li, J. Calcite U-Pb dating unravels the age and hydrothermal history of the giant Shuiyindong Carlin-type gold deposit in the golden triangle, South China. *Econ. Geol.* **2021**, *116*, 1253–1265. [\[CrossRef\]](#)
18. Zhang, F.X.; Chen, Y.J.; Li, C.; Zhang, J.; Ma, J.Q.; Li, X. Geological and geochemical characteristics and genesis of Jinlongshan-Qiuling gold deposit: Kinetic mechanism of Qinling Carlin-type gold deposit. *Sci. China* **2000**, *30*, 73–81. (In Chinese)
19. Liu, Y.H.; Li, Z.; Zhou, S.; Han, Y.Y.; Li, H.; Li, X.; Zhou, S.F. Geological characteristics, ore-forming ages and geological significance of Donggou-Jinlongshan gold deposit, South Qinling belt. *Earth Sci. Front.* **2016**, *23*, 81–93. (In Chinese)
20. Ma, Y.; Zhu, L.; Lu, R.; Ding, L.; Zhang, G.; Xiong, X.; Li, B. Geology and in-situ sulfur and lead isotope analyses of the Jinlongshan Carlin-type gold deposit in the Southern Qinling Orogen, China: Implications for metal sources and ore genesis. *Ore Geol. Rev.* **2020**, *126*, 103777. [\[CrossRef\]](#)
21. Dong, Y.; Santosh, M. Tectonic architecture and multiple orogeny of the Qinling Orogenic Belt, Central China. *Gondwana Res.* **2016**, *29*, 1–40. [\[CrossRef\]](#)
22. Tang, Y.Z.; Zhu, Z.W.; Wu, H.; Zhu, G.Z.; Wei, D.; Yao, S. Mineralization characteristics of submicron disseminated type gold deposits and dynamic metallogenic mechanism in Zhen'an-Xunyang basin, southern Qinling mountain belt. *Miner. Explor.* **2016**, *7*, 307–315.
23. Zhao, L.Q.; Deng, J.; Chen, X.; Zhou, H.; Li, X.M. Structural Control to the Genesis of Sediment-hosted Disseminated Jinlongshan Gold Orebelt, China. *Resour. Geol.* **2005**, *55*, 9–19. [\[CrossRef\]](#)
24. Zhao, X.K.; Cao, L.J.; Shen, Y.K.; Li, W.S.; Ma, Y.F.; Liu, Y.L.; Wang, X.H.; Sun, J.; Liu, L.M. The ore structural features and the ore-forming material source of the Shadonggou mercury antimony deposit in Xunyang, Shaanxi. *J. Geomech.* **2016**, *22*, 199–211. (In Chinese)
25. Xu, L.G.; Zheng, W. Contributions of Silurian black shales to the Pb-Zn mineralization in the Xunyang basin, southern Qinling. *Acta Geol. Sin.* **2021**, *95*, 1854–1867. (In Chinese)
26. Zhang, J.; Li, L.; Gilbert, S.; Liu, J.; Shi, W. LA-ICP-MS and EPMA studies on the Fe-S-As minerals from the Jinlongshan gold deposit, Qinling Orogen, China: Implications for ore-forming processes. *Geol. J.* **2014**, *49*, 482–500. [\[CrossRef\]](#)
27. Zhang, Y.; Chen, Y.J.; Qi, J.S.; Leng, C.B.; Zhao, C.H. Geochemistry of Gongguan-Qingtonggou Hg-Sb deposit in Xunyang, Shaanxi Province. *Acta Mineral. Sin.* **2010**, *30*, 98–106. (In Chinese)
28. Xiang, S. Geochemical Study on Ore-Forming Fluids of the Gongguan Hg-Sb Deposit in Xunyang Mansion, Shaanxi Province. Master's Thesis, Chinese Academy of China University of Geosciences, Beijing, China, 2020. (In Chinese).
29. Ma, Y.B. Metallogenesis of Gold, Mercury and Antimony Deposits in the Zhen'an-Xunyang Basin, South Qinling Orogen. Ph.D. Thesis, Chinese Academy of Northwest University, Xi'an, China, 2021. (In Chinese).
30. Yin, H.F.; Zhang, K.X. Evolution and characteristics of the Central Orogenic belt. *Earth Sci.-J. China Univ. Geosci.* **1998**, *23*, 437–442. (In Chinese)
31. Zhang, G.W. *Qinling Orogenic Belt and Continental Dynamics*; Beijing Science Press: Beijing, China, 2001; pp. 421–518. (In Chinese)
32. Zhang, G.W.; Meng, Q.J.; Lai, S.C. Structural structure of Qinling orogenic belt. *Sci. China* **1995**, *9*, 994–1003. (In Chinese)
33. Chen, Y.J.; Zhai, M.G.; Jiang, S.Y. Significant achievements and open issues in study of orogenesis and metallogenesis surrounding the North China Continent. *Acta Petrol. Sin.* **2009**, *25*, 2695–2726. (In Chinese)
34. Large, S.J.E.; Bakker, E.Y.N.; Weis, P.; Waelle, M.; Ressel, M.; Heinrich, C.A. Trace elements in fluid inclusions of sediment-hosted gold deposits indicate a magmatic-hydrothermal origin of the Carlin ore trend. *Geology* **2016**, *44*, 1015–1018. [\[CrossRef\]](#)
35. Zhu, H.P.; Ye, L.; Gan, B.X.; Wang, C.Q. The relationship to basin constructure system with metallogenic in Shan (yang)-Zha (shui)-Zhen (an)-Xun (yang) area. *Northwest. Geol.* **2003**, *36*, 52–58. (In Chinese)
36. Prokofiev, V.; Brovchenko, V.; Zorina, L.; Krasnov, A.; Abramova, V.; Bortnikov, N. Trace Elements in Pyrite and Its Crystallization Temperature: An Example of Gold Deposits in the Darasun Goldfield, Eastern Transbaikalia, Russia. *Minerals* **2023**, *13*, 288. [\[CrossRef\]](#)
37. Yan, G.S.; Ye, T.Z.; Pang, Z.S.; Xue, J.L.; Cheng, Z.Z.; Lu, Z.C.; Wei, C.S.; Wang, Y.W.; Zhu, X.Y.; Chen, H.; et al. Introduction of the theory and method of prospecting prediction of metallogenic geological body. *Geol. Bull. China* **2023**, *42*, 857–882. (In Chinese)
38. Wilson, S.A.; Ridley, W.I.; Koenig, A.E. Development of sulfide calibration standards for the laser ablation inductively-coupled plasma mass spectrometry technique. *J. Anal. At. Spectrosc.* **2002**, *17*, 406–409. [\[CrossRef\]](#)
39. Liu, Y.; Hu, Z.; Gao, S.; Günther, D.; Xu, J. In situ analysis of major and trace elements of anhydrous minerals by LA-ICP-MS without applying an internal standard. *Chem. Geol.* **2008**, *257*, 34–43. [\[CrossRef\]](#)

40. Bao, Z.; Chen, L.; Zong, C.; Yuan, H.; Chen, K.; Dai, M. Development of pressed sulfide powder tablets for in situ sulfur and lead isotope measurement using LA-MC-ICP-MS. *Int. J. Mass Spectrom.* **2017**, *255*–262. [\[CrossRef\]](#)
41. Chen, L.; Yuan, H.; Chen, K.; Bao, Z.; Zhu, L.; Liang, P. In situ sulfur isotope analysis by laser ablation MC-ICPMS and a case study of the Erlihe Zn-Pb ore deposit, Qinling orogenic belt, Central China. *J. Asian Earth Sci.* **2019**, *325*–336. [\[CrossRef\]](#)
42. Wang, C.; Shao, Y.; Huang, K.; Zhou, H.; Zhang, J.; Liu, Z.; Liu, Q. Ore-Forming Processes at the Xiajinbao Gold Deposit in Eastern Hebei Province: Constraints from EPMA and LA-ICPMS Analysis. *Minerals* **2018**, *8*, 388. [\[CrossRef\]](#)
43. Kudrin, M.V.; Fridovsky, V.Y.; Polufuntikova, L.I.; Kryuchkova, L.Y. Disseminated Gold–Sulfide Mineralization in Metasomatites of the Khangalass Deposit, Yana–Kolyma Metallogenic Belt (Northeast Russia): Analysis of the Texture, Geochemistry, and S Isotopic Composition of Pyrite and Arsenopyrite. *Minerals* **2021**, *11*, 403. [\[CrossRef\]](#)
44. Fridovsky, V.Y.; Polufuntikova, L.I.; Kudrin, M.V. Origin of Disseminated Gold-Sulfide Mineralization from Proximal Alteration in Orogenic Gold Deposits in the Central Sector of the Yana–Kolyma Metallogenic Belt, NE Russia. *Minerals* **2023**, *13*, 394. [\[CrossRef\]](#)
45. Bralía, A.; Sabatini, G.; Troja, F. A reevaluation of the Co/Ni ratio in pyrite as geochemical tool in ore genesis problems; evidences from southern Tuscany pyritic deposits. *Miner. Depos.* **1979**, *14*, 353–374. [\[CrossRef\]](#)
46. Román, N.; Reich, M.; Leisen, M.; Morata, D.; Barra, F.; Deditius, A.P. Geochemical and micro-textural fingerprints of boiling in pyrite. *Geochim. Cosmochim. Acta* **2019**, *246*, 60–85. [\[CrossRef\]](#)
47. Lee, M.; Shin, D.; Yoo, B.; Im, H.; Pak, S.; Choi, S. LA-ICP-MS trace element analysis of arsenopyrite from the Samgwang gold deposit, South Korea, and its genetic implications. *Ore Geol. Rev.* **2019**, *114*, 103147. [\[CrossRef\]](#)
48. Morishita, Y.; Shimada, N.; Shimada, K. Invisible gold in arsenian pyrite from the high-grade Hishikari gold deposit, Japan: Significance of variation and distribution of Au/As ratios in pyrite. *Ore Geol. Rev.* **2018**, *95*, 79–93. [\[CrossRef\]](#)
49. Zhang, H.; Cai, Y.; Sha, G.; Brugger, J.; Pring, A.; Ni, P.; Qian, G.; Luo, Z.; Zhang, Y.; Tan, W. Effects of arsenic on the distribution and mode of occurrence of gold during fluid-pyrite interaction: A case study of pyrite from the Qiucun gold deposit, China. *Am. Mineral.* **2022**, *107*, 914–929. [\[CrossRef\]](#)
50. Gopon, P.; Douglas, J.O.; Auger, M.A.; Hansen, L.; Wade, J.; Cline, J.S.; Robb, L.J.; Moody, M.P. A Nanoscale Investigation of Carlin-Type Gold Deposits: An Atom-Scale Elemental and Isotopic Perspective. *Econ. Geol.* **2019**, *114*, 1123–1133. [\[CrossRef\]](#)
51. Wu, Y.; Fougereuse, D.; Evans, K.; Reddy, S.M.; Saxey, D.W.; Guagliardo, P.; Li, J. Gold, arsenic, and copper zoning in pyrite: A record of fluid chemistry and growth kinetics. *Geology* **2019**, *47*, 641–644. [\[CrossRef\]](#)
52. Reich, M.; Kesler, S.E.; Utsunomiya, S.; Palenik, C.S.; Chryssoulis, S.L.; Ewing, R.C. Solubility of gold in arsenian pyrite. *Geochim. Cosmochim. Acta* **2005**, *69*, 2781–2796. [\[CrossRef\]](#)
53. Deditius, A.P.; Utsunomiya, S.; Renock, D.; Ewing, R.C.; Ramana, C.V.; Becker, U.; Kesler, S.E. A proposed new type of arsenian pyrite: Composition, nanostructure and geological significance. *Geochim. Cosmochim. Acta* **2008**, *72*, 2919–2933. [\[CrossRef\]](#)
54. Deditius, A.P.; Utsunomiya, S.; Ewing, R.C.; Kesler, S.E. Nanoscale “liquid” inclusions of As-Fe-S in arsenian pyrite. *Am. Mineral.* **2009**, *94*, 391–394. [\[CrossRef\]](#)
55. Reich, M.; Utsunomiya, S.; Kesler, S.E.; Wang, L.; Ewing, R.C.; Becker, U. Thermal behavior of metal nanoparticles in geologic materials. *Geology* **2006**, *34*, 1033–1036. [\[CrossRef\]](#)
56. Blanchard, M.; Alfredsson, M.; Brodholt, J.; Wright, K.; Catlow, C.R.A. Arsenic incorporation into FeS₂ pyrite and its influence on dissolution: A DFT study. *Geochim. Cosmochim. Acta* **2007**, *71*, 624–630. [\[CrossRef\]](#)
57. Yang, R.S.; Chen, Y.J.; Xie, J.L. X-ray photoelectron spectroscopic study on arsenian pyrite and arsenopyrite from the Yangshan gold deposit, Gansu province (North China). *Acta Petrol. Sin.* **2009**, *25*, 2791–2800. (In Chinese)
58. Qian, G.; Brugger, J.; Testemale, D.; Skinner, W.; Pring, A. Formation of As(II)-pyrite during experimental replacement of magnetite under hydrothermal conditions. *Geochim. Cosmochim. Acta* **2013**, *100*, 1–10. [\[CrossRef\]](#)
59. Meng, W.Y.; Liu, J.J.; Wei, L.Y.; Zhang, Z.; Wu, H.H.; Fan, B.C.; Pan, Y.; Li, G.Y.; Jia, B. Sulfur and Lead Isotope Compositions of the Xiaohu Gold Deposit at Xunyang, Shaanxi Province, and its Geological Significance. *Geoscience* **2021**, *35*, 1587–1596. (In Chinese)
60. Gadd, M.G.; Layton-Matthews, D.; Peter, J.M.; Paradis, S.; Jonasson, I.R. The world-class Howard’s Pass SEDEX Zn-Pb district, Selwyn Basin, Yukon. Part II: The roles of thermochemical and bacterial sulfate reduction in metal fixation. *Miner. Depos.* **2017**, *52*, 405–419. [\[CrossRef\]](#)
61. Qiu, W.J.; Zhou, M.; Li, X.; Williams-Jones, A.E.; Yuan, H. The Genesis of the Giant Dajiangping SEDEX-Type Pyrite Deposit, South China. *Econ. Geol.* **2018**, *113*, 1419–1446. [\[CrossRef\]](#)
62. Chang, Z.; Large, R.R.; Maslennikov, V. Sulfur isotopes in sediment-hosted orogenic gold deposits; evidence for an early timing and a seawater sulfur source. *Geology* **2008**, *36*, 971–974. [\[CrossRef\]](#)
63. Wei, D.; Xia, Y.; Gregory, D.D.; Steadman, J.A.; Tan, Q.; Xie, Z.; Liu, X. Multistage pyrites in the Nibao disseminated gold deposit, southwestern Guizhou Province, China: Insights into the origin of Au from textures, in situ trace elements, and sulfur isotope analyses. *Ore Geol. Rev.* **2020**, *122*, 103446. [\[CrossRef\]](#)
64. Kelley, D.L.; Kelley, K.D.; Coker, W.B.; Caughlin, B.; Doherty, M.E. Beyond the obvious limits of ore deposits; the use of mineralogical, geochemical, and biological features for the remote detection of mineralization. *Econ. Geol. Bull. Soc. Econ. Geol.* **2006**, *101*, 729–752. [\[CrossRef\]](#)
65. Richards, J.P. Postsubduction porphyry Cu-Au and epithermal Au deposits; products of remelting of subduction-modified lithosphere. *Geology* **2009**, *37*, 247–250. [\[CrossRef\]](#)
66. Richards, J.P. Hidden gold. *Nat. Geosci.* **2011**, *4*, 73–74. [\[CrossRef\]](#)
67. Sillitoe, R.H.; Meinert, L.D. Porphyry copper systems. *Econ. Geol. Bull. Soc. Econ. Geol.* **2010**, *105*, 3–41. [\[CrossRef\]](#)

68. Xie, G.; Mao, J.; Wang, R.; Ren, T.; Li, J.; Da, J. Origin of Late Mesozoic granitoids in the newly discovered Zha-Shan porphyry Cu district, South Qinling, central China, and implications for regional metallogeny. *J. Asian Earth Sci.* **2015**, *103*, 184–197. [[CrossRef](#)]
69. Xie, X.; Fu, Y.; Liu, J. Mineralogical characteristic of ductile-brittle shear zone in the Baguamiao gold deposit, Shaanxi Province: Implication for gold mineralization. *Geol. J.* **2017**, *52*, 81–96. [[CrossRef](#)]
70. Chen, L.; Yan, Z.; Wang, Z.; Wang, K. Petrogenesis of Early Cretaceous dioritic dikes in the Shanyang-Zhashui area, South Qinling, Central China: Evidence for partial melting of thickened lower continental crust. *J. Asian Earth Sci.* **2018**, *158*, 324–335. [[CrossRef](#)]
71. Xiong, X.; Zhu, L.; Zhang, G.; Guo, A.; Zheng, J.; Jiang, H. Origin of the Xiaohekou skarn copper deposit and related granitoids in the Zha-Shan ore cluster area, South Qinling, China. *Ore Geol. Rev.* **2019**, *114*, 103143. [[CrossRef](#)]
72. Xiong, X.; Zhu, L.; Zhang, G.; Zheng, J.; Jiang, H. Insights into the skarn Cu mineralization processes of an intracontinental setting: A case study of the Xiaohekou deposit, southern Qinling Orogen, China. *J. Geochem. Explor.* **2021**, *230*, 106862. [[CrossRef](#)]
73. Ding, K. Metallogenesis and Metallogenic Dynamics Background of Typical Gold Deposits in Zha-shan Ore Concentration Area, South Qinling. Ph.D. Thesis, Chinese Academy of Chang'an University, Xi'an, China, 2020. (In Chinese).
74. Liu, K.; Wang, R.T.; Fan, Z.P.; Ren, T.; Li, J.B.; Zhao, L.; Zhao, X.L.; Xiao, P.H. Metallogenic age of Xiajiadian gold deposit in the Zhashui-Shanyang ore concentration, Qinling orogenic belt and its geological significance. *Miner. Depos.* **2019**, *38*, 1278–1296. (In Chinese with English abstract)
75. Arehart, G.B.; Chakurian, A.M.; Tretbar, D.R.; Christensen, J.N.; McInnes, B.A.; Donelick, R.A. Evaluation of radioisotope dating of Carlin-type deposits in the Great Basin, western North America, and implications for deposit genesis. *Econ. Geol. Bull. Soc. Econ. Geol.* **2003**, *98*, 235–248.
76. Cline, J.S.; Hofstra, A.H.; Muntean, J.L.; Tosdal, R.M.; Hickey, K.A. Carlin-Type Gold Deposits in Nevada Critical Geologic Characteristics and Viable Models. In *One Hundredth Anniversary*; Society of Economic Geologists: Littleton, CO, USA, 2005; Volume 2005. [[CrossRef](#)]
77. Meng, Q.Z.; Zhang, G.W.; Yu, Z.P. Carboniferous tectono-sedimentary environment of Qinling subduction plate front. *J. Earth Sci. Environment* **1993**, *15*, 5. (In Chinese)
78. Yin, H.F.; Yang, F.Q.; Huang, Q.S. *The Triassic of Qinling Mountains and Neighboring Areas*; China University of Geosciences Press: Wuhan, China, 1992; pp. 12–107. (In Chinese)
79. Yin, H.F.; Du, Y.S.; Xu, J.F.; Sheng, J.H.; Feng, Q.L. Discovery of radiolarian fauna and its paleo marine significance in Mian-Lue suture zone of South Qinling. *Earth Sci.* **1996**, *21*, 184. (In Chinese)

Disclaimer/Publisher's Note: The statements, opinions and data contained in all publications are solely those of the individual author(s) and contributor(s) and not of MDPI and/or the editor(s). MDPI and/or the editor(s) disclaim responsibility for any injury to people or property resulting from any ideas, methods, instructions or products referred to in the content.